ACS OMEGA

http://pubs.acs.org/journal/acsodf

Article

Interactions of Urea-Based Inhibitors with Prostate-Specific Membrane Antigen for Boron Neutron Capture Therapy

Qiaoyu Hu, Kevin Padron, Daiki Hara, Junwei Shi, Alan Pollack, Rajeev Prabhakar,* and Wensi Tao*

Cite This: *ACS Omega* 2021, 6, 33354−33369

Read Online

ACCESS | Metrics & More | Article Recommendations | Supporting Information

ABSTRACT: In this study, molecular interactions of prostate-specific membrane antigen (PSMA) with five chemically distinct urea-based boron-containing inhibitors have been investigated at the atomic level using molecular docking and molecular dynamics simulations. The PSMA−inhibitor complexations have been analyzed by comparing their binding modes, secondary structures, root-mean-square deviations, noncovalent interactions, principal components, and binding free energies. PSMA is a cell surface glycoprotein upregulated in cancerous cells and can be targeted by boron-labeled inhibitors for boron neutron capture therapy (BNCT). The effective BNCT requires the selective boron delivery to the tumor area and highly specific PSMA-mediated cellular uptake by tumor. Thus, a potent inhibitor must exhibit both high binding affinity and high boron density. The computational results suggest that the chemical nature of inhibitors affects the binding mode and their association with PSMA is primarily dominated by hydrogen bonding, salt bridge, electrostatic, and $\pi-\pi$ interactions. The binding free energies (−28.0, −15.2, −43.9, −23.2, and −38.2 kcal/mol) calculated using λ-dynamics for all inhibitors (**In1−5**) predict preferential binding that is in accordance with experimental data. Among all inhibitors, **In5** was found to be the best candidate for BNCT. The binding of this inhibitor to PSMA preserved its overall secondary structure. These results provide computational insights into the coordination flexibility of PSMA and its interaction with various inhibitors. They can be used for the design and synthesis of efficient BNCT agents with improved drug selectivity and high boron percentage.

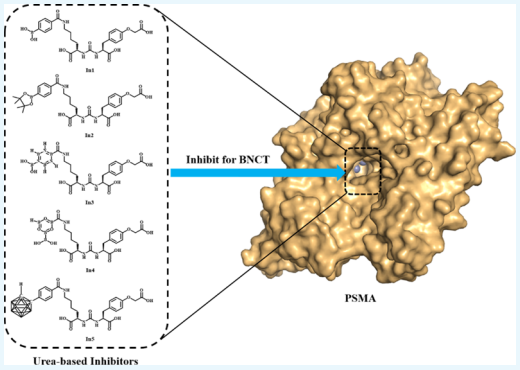

I. INTRODUCTION

Boron neutron capture therapy (BNCT) is a noninvasive two-step cancer treatment modality utilizing the nuclear fission reaction when neutrons are captured by the boron-10 isotope (B^{10}).[1] The first step is the selective delivery of B^{10}-containing chemicals to the tumor cells; the second step is the irradiation of the boron-loaded tumor area with either a thermal or an epithermal neutron beam.[2,3] Irradiation with a high flux neutron beam results in the emission of lithium ions and high linear energy transfer (LET) alpha particles, which travel less than 10 μm in human tissues.[1] The ability of B^{10} to release high LET alpha particles at such a short distance, approximately the diameter of a cell, enables the focal deposition of ionizing radiation energy selectively to the tumor area while sparing surrounding normal tissues.[4] The boron-containing compounds for BNCT should have these two properties: (1) selective uptake by tumor cells to achieve a high concentration of absorbed neutrons in tumor. (2) Rapid clearance from circulation and normal tissues with low systemic toxicity.[5]

The main challenges for developing an ideal BNCT reagent are to achieve relatively high tumor-specific uptake (more than 20 μg/g tumor) and low normal tissue toxicity.[6] Within the short period of time between infusion and neutron irradiation, boron-containing reagents need to maintain a high concentration in the tumor area, and after that, they should be quickly cleared from normal tissue and circulation.[3,5,6] Currently, 4-borono-L-phenylalanine (BPA) and sodium borocaptate (BSH) are two clinically used BNCT reagents.[7−9] The major limitation with both BPA and BSH is the relatively low tumor-to-normal tissue ratio because of the variability in tumor uptake.[10] Due to these disadvantages, clinical usage of BNCT has been mainly limited to patients with high-grade gliomas or recurrent head and neck cancers which do not respond to conventional therapy.[11−14] For other types of cancers, BNCT is still not applied as the first-line standard of care therapy.[15] Recently, several tumor targeting strategies have been incorporated to improve the efficiency of boron delivery and retention using unnatural amino acids, peptides, proteins, sugars, and nanoparticles.[6,16,17] A couple of cell surface

Received: July 6, 2021
Accepted: October 4, 2021
Published: December 1, 2021

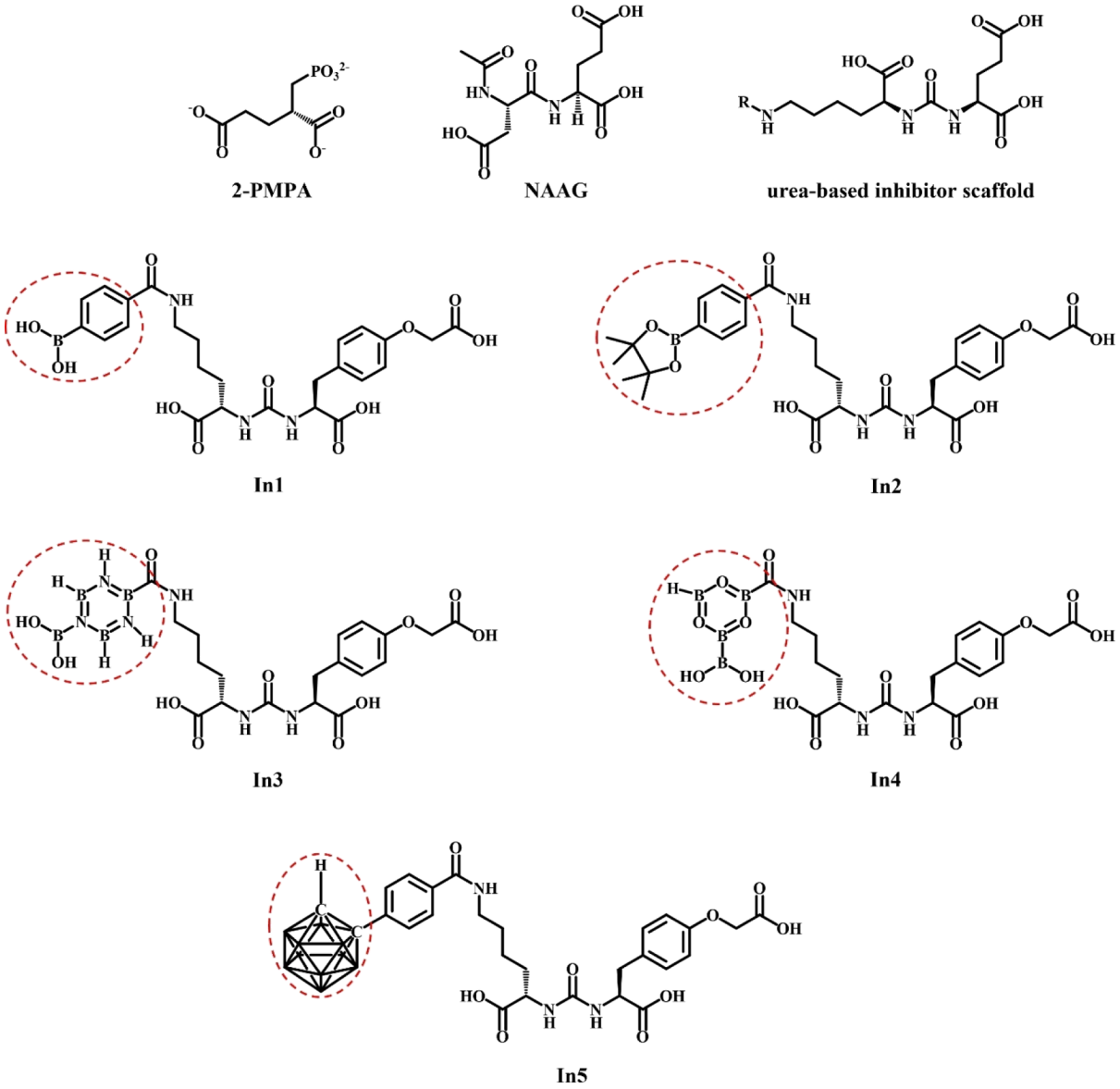

Figure 1. Chemical structures of 2-PMPA, NAAG, urea-based inhibitor scaffold, and boron-containing inhibitors (In1−In5).

receptors that overexpressed on tumors have been utilized as targets for developing boron-containing ligands.[18] These receptors include the vascular endothelial growth factor receptor (VEGFR), somatostatin receptors, thymidine kinase 1, and the epidermal growth factor receptor (EGFR).[19−22] Targeted delivery of BNCT reagents such as boronated VEGFR, EGFR, and anti-EGFR monoclonal antibodies have been used in tumor vasculature and EGFR-positive glioma.[19−21]

Prostate-specific membrane antigen (PSMA), also called glutamate carboxypeptidase II (GCPII), is a 750-amino-acid-residue-containing class II transmembrane metalloenzyme, which possesses a dinuclear zinc core at the active site.[23−25] Encoded by the humans' *FOLH1* (folate hydrolase (1) gene,[26] PSMA is expressed in many tissues including the prostate, kidney, liver, intestinal epithelium, and central nervous system,[27,28] and it plays distinct biological roles in different tissues. In the intestine, the *FOLH1* gene is associated with impaired dietary folate absorption, which can lead to conditions such as a low blood folate level and hyperhomocysteinemia.[29,30] In the central nervous system, *N*-acetyl-L-aspartyl-L-glutamate (NAAG) is hydrolyzed by PSMA into *N*-acetylaspartate (NAA) and glutamate (Glu), which is a neurotransmitter that relates to neurotoxicity and neuronal death in the brain at enhanced levels.[31−33] In addition, PSMA expression is upregulated in cancerous cells and used as an effective diagnostic and prognostic indicator for prostate cancer.[34] The expression of PSMA is observed both in primary and metastatic prostate cancer. Its expression levels correlate positively as prostate cancer develops into high-grade and metastatic cancer.[35] Interestingly, PSMA expression is also regulated by the androgen receptor (AR).[36] Androgen deprivation therapy such as enzalutamide can upregulate the PSMA expression level in castration-resistant prostate cancer.[37]

As an independent diagnostic/prognostic marker, PSMA ligands (especially those labeled with Gallium-68 and Fluor-18) have been extensively applied in positron emission tomography/computed tomography (PET/CT) for oligometastatic prostate cancer imaging.[38−40]

https://doi.org/10.1021/acsomega.1c03554
ACS Omega 2021, 6, 33354−33369

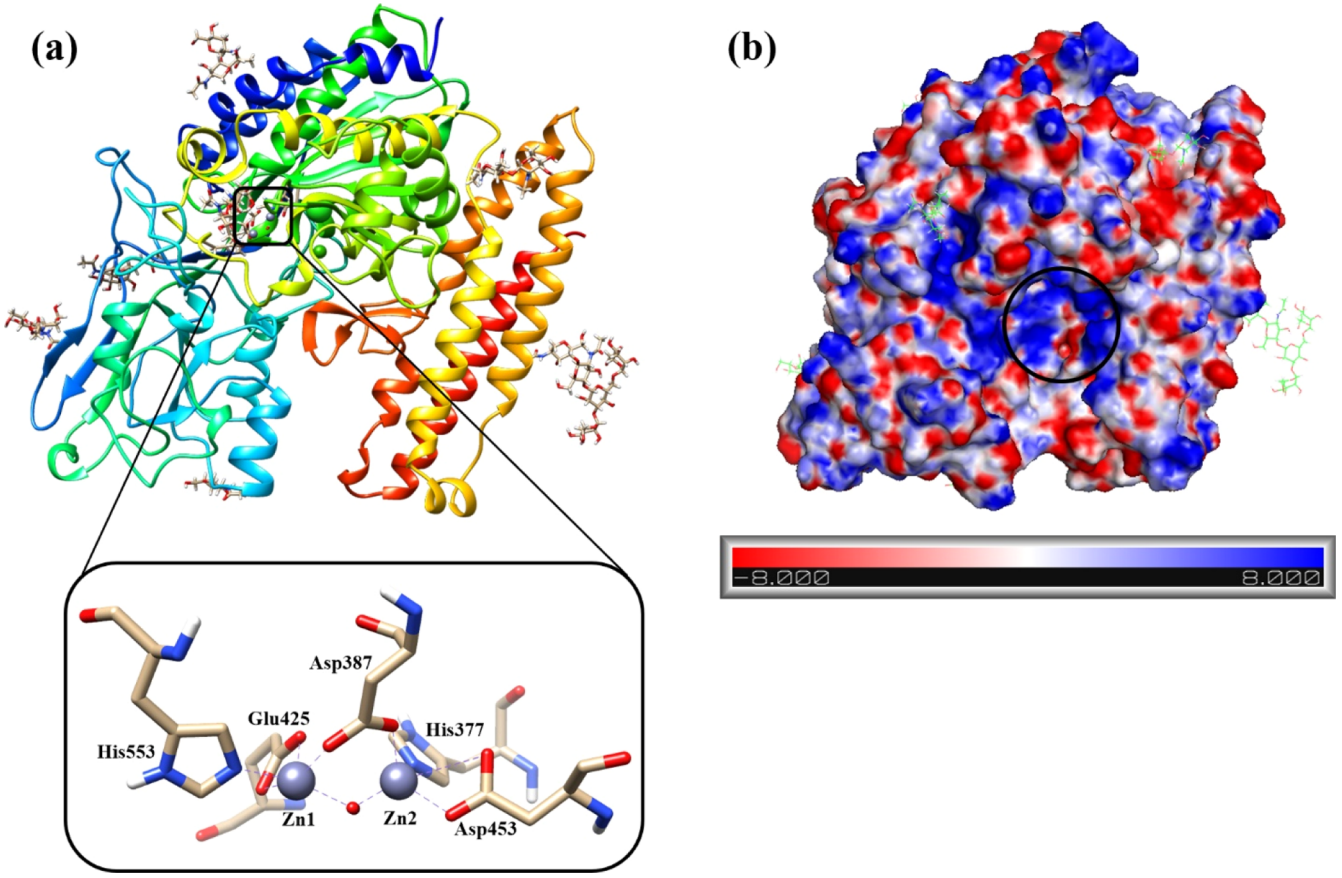

Figure 2. (a) Crystal structure of PSMA and its binuclear active site and (b) ESP of PSMA.

In 2021, the U.S. Food and Drug Administration (FDA) has approved 177Lu-PSMA-617, a PSMA-targeted radioligand therapy for the treatment of metastatic castration-resistant prostate cancer (mCRPC). Although therapy with 177Lu-PSMA-617 demonstrated successful tumor control, it also exhibits side effects such as xerostomia and bone marrow suppression.[41,42] Unlike 177Lu-PSMA-617 that allows PSMA-labeled radioisotopes to be concentrated within the cell, boron-10-containing compounds are nonradioactive inhibitors with low toxicity. Important organs such as the heart, kidney, liver, and lungs can be protected by avoiding dose to the tissues outside the irradiation field. Therefore, a treatment of prostate cancer with PSMA-targeting BNCT reagents may be a promising strategy for highly specific tumor delivery as it produces minimum side effects and toxicity for normal tissues. PSMA can be targeted by various molecular agents, which can be categorized into several classes: small molecules,[43] small peptides,[44] polymers,[45,46] nanoparticles,[47,48] and monoclonal antibodies.[49,50] In comparison to other reagents, small molecules and peptides can easily circulate in the blood stream through the major organs including the tumor site within a few hours because of their smaller size.[51] After 24−36 h, they can also be rapidly eliminated from the plasma by excreting into urine through the kidney. In contrast, when monoclonal antibodies against PSMA are injected, the tumor-to-normal tissue signal ratio takes around 24 h to reach its peak and can last as long as 72−120 h[52] because these antibodies possess higher molecular weight, longer stability in blood-stream, and stronger binding affinity. Therefore, smaller molecules are proposed to be the promising reagents for BNCT on account of their quicker delivery to the tumor region and shorter half-lives in the circulation system.

The X-ray structure of PSMA has been resolved at 1.84 Å resolution (PDB ID: 4NGM).[24,53] In this structure, the zinc-containing active site is located at a depth of approximately 20 angstrom (Å) from the surface.[24] The whole cavity around the active site can be separated into two substrate binding sites: S1′ site and S1 site, which accommodate the P1′ and P1 portions of inhibitors, respectively. It has been established that the S1′ site is more specific to glutamate residue or glutamate analogues, whereas the S1 site is more flexible and can accommodate different molecules.[24,25,54−57] PSMA ligands can be classified into two categories (Figure 1): the first class is the phosphorus-based ligands mimicking the transition state of hydrolytic reaction and the second class is urea-based inhibitors with the hydrolysis-resistant peptide bond surrogate.[58−60] The urea-based inhibitors can bind to both S1′ and S1 sites like the NAAG, which is the natural substrate of PSMA.[61] They provide several advantages such as an ease of large-scale synthesis, penetration of the blood−brain barrier, and radiolabeling.[62,63] The unique chemical properties of these urea derivatives result in their better tumor uptake and higher binding affinity to a lipophilic pocket located near the active site of PSMA.[64] Moreover, the urea-based scaffold is also very tolerant with regard to structural modification. Therefore, these inhibitors can be exploited not only as diagnostic tools for PSMA-targeted molecular imaging but also as radiolabeled small molecules to treat advanced prostate cancer.[65]

Previously reported PSMA-targeted BNCT compounds were mostly based upon the urea scaffold. Due to high

https://doi.org/10.1021/acsomega.1c03554
ACS Omega 2021, 6, 33354−33369

boron content, a series of carborane derivatives have been synthesized and evaluated for inhibitory activity, tumor uptake, and biodistribution.[60,66,67] In this study, we aim to computationally analyze the interactions between PSMA and potential boron-containing PSMA-targeted inhibitors, which are proposed according to previous urea-based molecules and a structure−activity relationship (SAR) study.[56] In order to be clinically effective agents for BNCT, the PSMA inhibitors must possess high tumor-to-normal tissue ratios, high binding affinities, and high boron densities. A deeper understanding of interactions between the PSMA and inhibitors at the atomistic level will facilitate this goal.

II. Results and Discussion. The crystal structure of PSMA and its active site are displayed in Figure 2a. The bulk part (707 residues) of this enzyme resides in extracellular space, and the remaining part includes a short cytoplasmic N-terminal region (19 residues) and a single membrane-spanning segment (24 residues).[24,68] The extracellular part of this enzyme can be divided into three distinct domains (protease domain, apical domain, and C-terminal domain), all of which are involved in substrate recognition and binding. The protease domain (domain I, 57−116 and 352−590 residues, green color in Figure 2a) is mainly composed of seven central β sheets with 10 flanking α helices, whereas the apical domain (domain II, 117−351 residues, cyan color in Figure 2a) forms a deep funnel-shaped tunnel, from which the substrate can enter the active site (20 Å away from the protein surface). The C-terminal domain (domain III, 591−750 residues, orange color in Figure 2a) is constituted by four α helical bundles with an up-down-up-down order.[24,68] Under the physiological conditions, PSMA tends to exist as an active homodimer, whose dimerization interface is stabilized by the interactions between domain I/II of one monomer and domain III of another.[55]

Harbored in the protease domain, the active site of PSMA (Figure 2a) contains two zinc metal ions, designated as Zn1 and Zn2. Among them, Zn1 interacts with Asp387, Glu425, and His553, while Zn2 is ligated to His377, Asp387, and Asp453. Glu425 and Asp453 coordinate to Zn1 and Zn2, respectively, in a bidentate binding mode. Additionally, Asp387 and a hydroxyl group (μOH) bridge both metal ions. The metal−metal and metal−ligand distances are summarized in Table 1. The electrostatic surface potential (ESP) indicates that the funnel-shaped tunnel (black circle in Figure 2b) is largely composed of positive charges. The chemical structures of urea-based inhibitors are shown in Figure 1. The urea-based scaffold is linked to distinct boron ligands through an aromatic or an aliphatic chain. The number of boron atoms in these inhibitors gradually increases from 1 to 10 to fulfill a key requirement for effective BNCT (at least 20−50 μg of boron uptake per g of tumor).[3]

In this study, we investigated the interactions of PSMA with five chemically distinct urea-based boron-containing inhibitors (**In1**−**In5**) at the atomic level using molecular dynamics (MD) simulations. The structures of all complexes (**PSMA**−**In1**, **PSMA**−**In2**, **PSMA**−**In3**, **PSMA**−**In4**, and **PSMA**−**In5**) and their interactions are discussed using their binding modes, secondary structures, root-mean-square deviations (RMSD), noncovalent interactions (NCIs), principal components, and binding free energies as parameters.

IIa. PSMA−In1 Interactions. Since SAR study[56] suggested that P1′ and P1 parts of inhibitors preferred bulky groups, a phenyl moiety is introduced at both positions. As a consequence, the glutamate analogue with a phenyl ring of tyrosine occupies the P1′ segment and the lysine analogue with a phenyl ring of benzene resides in the P1 position. For Inhibitor1 (**In1**), a boronic acid (shown in the circle in Figure 1) is attached to the phenyl ring of the P1 portion to form a phenylboronic acid. As shown in Figure 3a, the binding of **In1** to the active site is predominately propelled by the interactions between two positively charged zinc metal ions and negatively charged oxygen atoms of the inhibitor. Specifically, the carbonyl oxygen of ureido linkage coordinates to Zn1 at a distance of 2.15 Å and one oxygen of the carboxylate group from P1 connects to Zn2 with a distance of 2.19 Å, resulting in a μ-1,6 bidentate mode. The bridging hydroxide μ-OH shifts to a more symmetrical position (1.91 Å (Zn1) and 1.90 Å (Zn2), Table 1) and the metal−metal distance is elongated by 0.19 Å upon inhibitor binding, which is consistent with experimental observations.[24,68] All ligands surrounding Zn^{2+} ions (six-coordinated) adopt a distorted octahedral geometry. The boronic acid that links to the aromatic moiety of P1 points to the opposite direction of the funnel-shaped tunnel, protruding into a pocket enclosed by Arg210 and Tyr234. The RMSD value derived from the superposition (Figure 3b) of equilibrated and crystallographic structures of the active site is only 0.61 Å, substantiating the validity of our MD simulations. Furthermore, the RMSD plot (Figure 4a) for the α carbon of the enzyme indicates that the simulation of the **PSMA**−**In1** complex achieves equilibrium at around 40 ns. This equilibrium is further confirmed by the pairwise RMSD plot (Figure S1a) that calculates the RMSD value of each frame to all other frames in the trajectory. Dominating fluctuations focus on the S1′ site and C-terminal loop, whereas the S1 site and the first coordination shell experience less fluctuations (Figure 4b). It also exhibits the rigidity of the S1′ site and flexibility of the S1 site. The PCA of the **PSMA**−**In1** complex (Figure 3c) displays a V-shaped graph accompanied with a variety of narrow spread energy basins, manifesting the existence of multiple ensemble conformations. A similar PCA graph is also observed in the MD simulation of glycerolphos-

Table 1. Metal Coordination Number and Metal−Metal, Metal−Substrate, Metal−OH, and Metal−Ligand Distances (Å) for the First Coordination Shell Residues in the PSMA Crystal and Equilibrated Structures (Inhibitors 1 and 2) and the Calculated Binding Free Energies of Distinct Inhibitors (kcal/mol)[a]

	PSMA crystal	PSMA−In1	PSMA−In2
coordination number	5(Zn1), 4(Zn2)	6(Zn1), 6(Zn2)	6(Zn1), 6(Zn2)
$M_{Zn1}-M_{Zn2}$	3.26	3.45	3.55
inhibitor		2.15(Zn1), 2.19(Zn2)	2.19(Zn1)
μOH	2.08(Zn1), 1.68(Zn2)	1.91(Zn1), 1.90(Zn2)	1.88(Zn1), 1.91(Zn2)
His377	1.98(Zn2)	2.15(Zn2)	2.14(Zn2)
Asp387	1.98(Zn1), 2.03(Zn2)	2.23(Zn1), 2.08(Zn2)	2.24(Zn1), 2.12(Zn2)
Glu424	3.73(Zn2)	5.84(Zn2)	2.20(Zn2)
Glu425	2.17, 2.42(Zn1)	2.12, 2.09(Zn1)	2.21, 2.14(Zn1)
Asp453	2.02, 2.91(Zn2)	2.19, 2.11(Zn2)	2.26, 2.21(Zn2)
His553	2.04(Zn1)	2.11(Zn1)	2.21(Zn1)
binding free energy		−28.0	−15.2

[a]Metal coordination sites (Zn1 and Zn2) are shown in the parentheses.

https://doi.org/10.1021/acsomega.1c03554
ACS Omega 2021, 6, 33354−33369

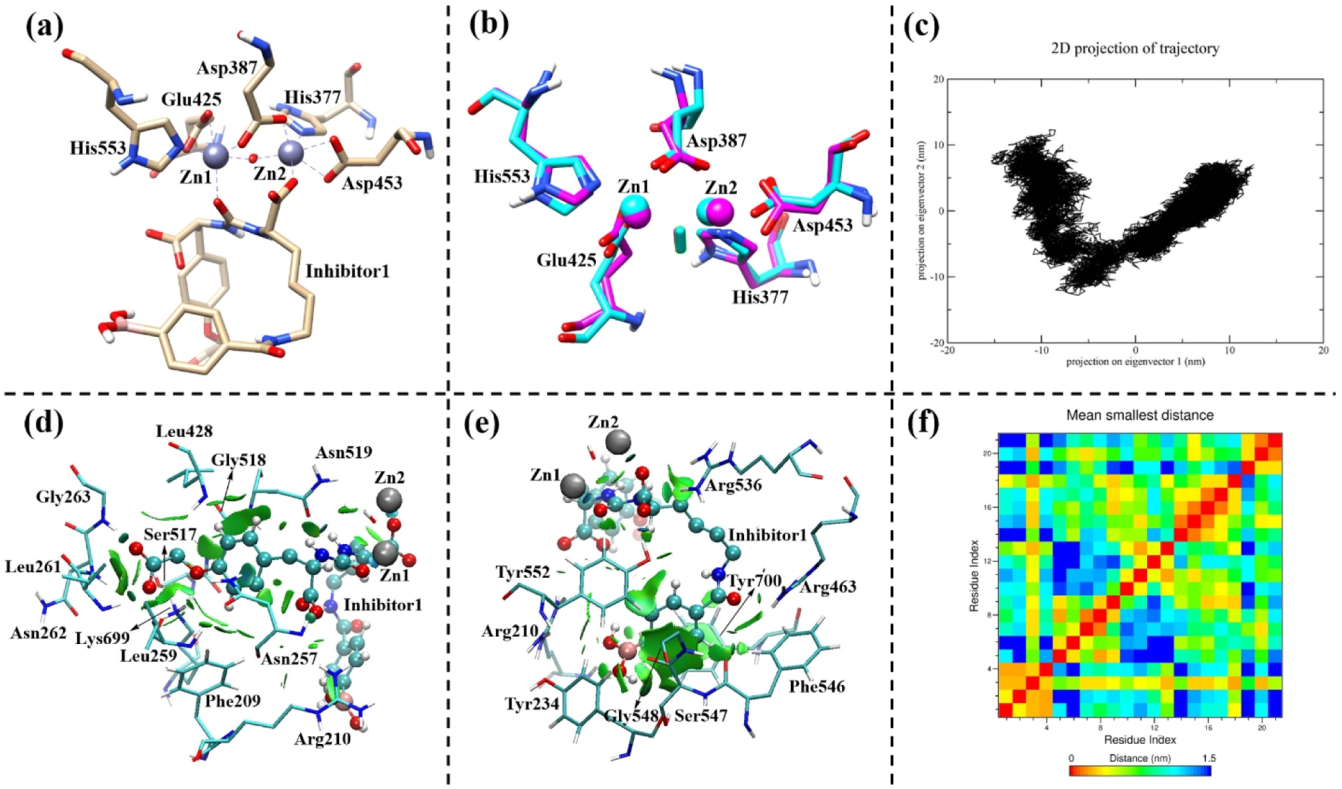

Figure 3. Most representative structure of the **PSMA−In1** complex derived from MD simulations: (a) active site with the inhibitor, (b) superposition of the active site of the equilibrated structure (magenta carbon) and crystal structure (cyan carbon), (c) principal component analysis, (d) NCI plot of the S1′ site with amino acid residues labeled, (e) NCI plot of the S1 site with amino acid residues labeled, and (f) contact map of the S1 site.

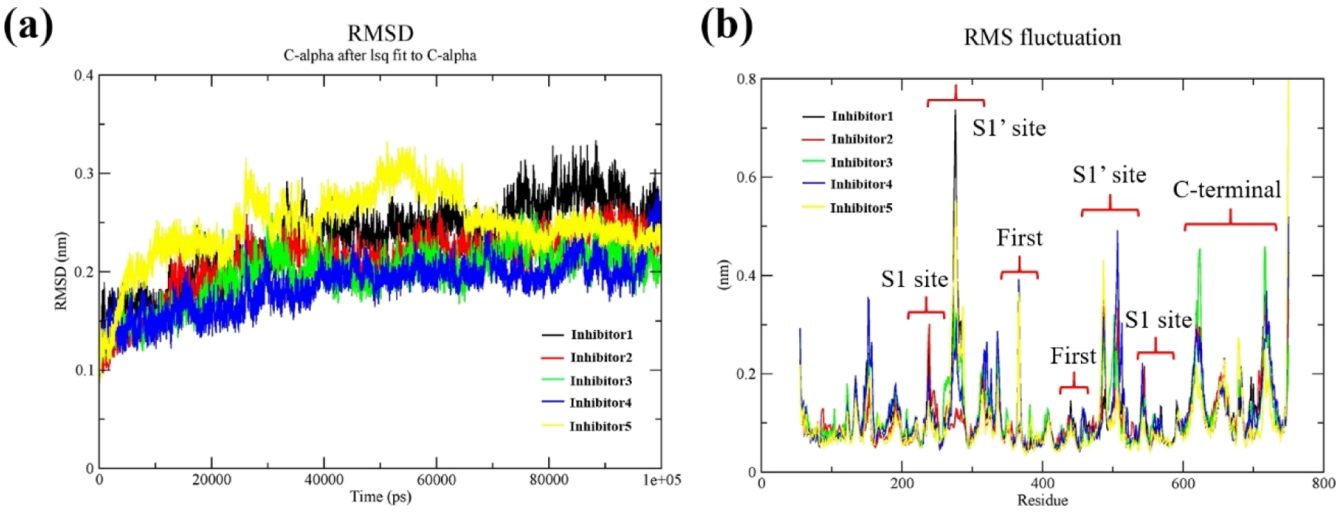

Figure 4. (a) RMSD of all complexes and (b) root-mean-square fluctuations of all complexes.

phodiesterase (GpdQ) combined with the paraoxon substrate.[69,70]

The glutamate analogue of **In1** occupies the S1′ pocket, which is composed of 12 amino acid residues. These residues are highlighted as the primary source of interaction by the NCI contour plot (Figures 3d and S2a). The α-carboxylic group of **In1** at the S1′ site forms a salt bridge and a hydrogen bond with the guanidinium moiety (N^{η}) of Arg210 and the backbone amino group of Asn257 at distances of 2.89 and 1.99 Å, respectively. The aromatic ring interacts with the γ-amino group (N^{δ}) of Asn257 and the side chain of Phe209 through NH−π and T-shaped π−π interactions, respectively. Overall, the substrate binding mode of **In1** in the S1′ site is analogous to those of the PSMA complex with GPI-18431[24] and 2-PMPA,[68] both of which possess the exact glutamate in their structures. Typically, Lys699 and Tyr700 are denominated as the "glutarate sensor" to recognize two carboxylate groups of glutarate in the substrate via the induced-fit mechanism.[24,68] When there are no substrates, these two residues are located outside the S1′ site, while in the presence of the substrate, they enter the S1′ site and principally select glutarate-like structures. However, in the equilibrated structure

https://doi.org/10.1021/acsomega.1c03554
ACS Omega 2021, 6, 33354−33369

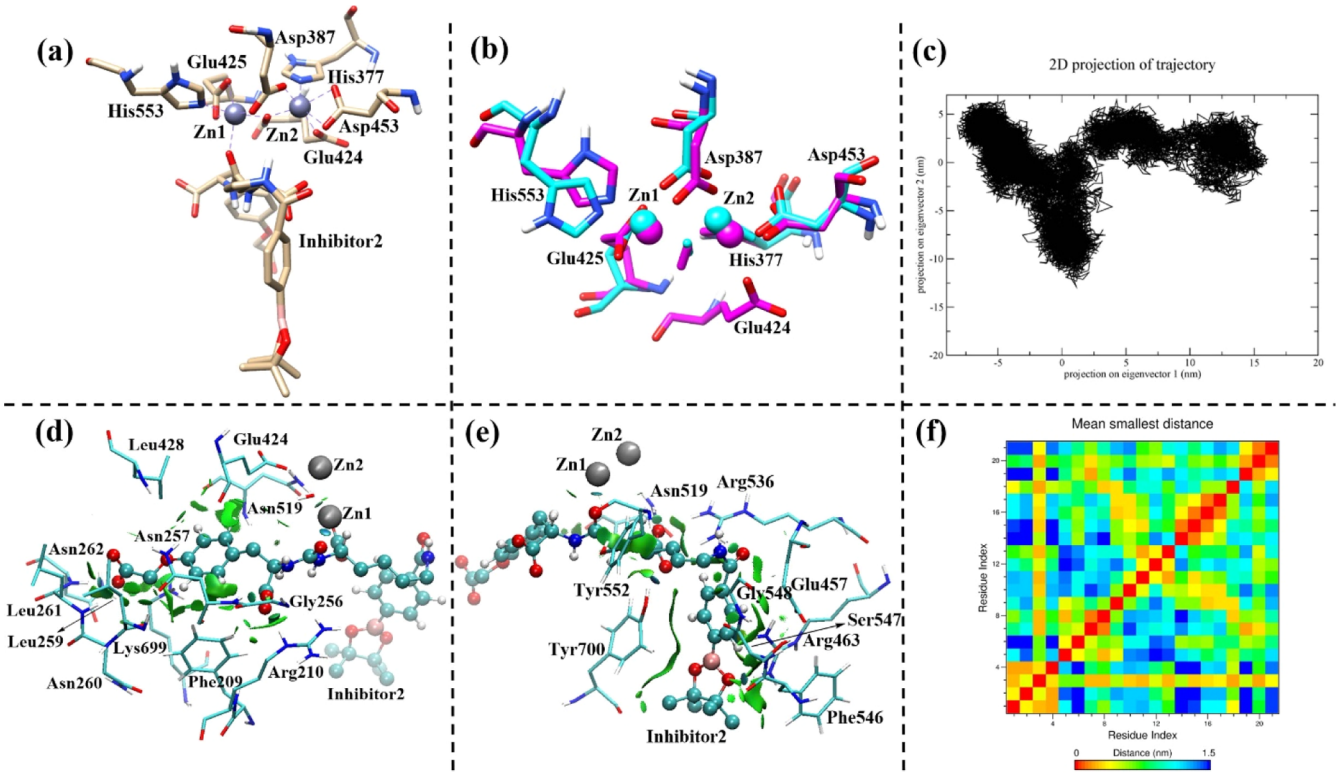

Figure 5. Most representative structure of the **PSMA−In2** complex derived from MD simulations: (a) active site with the inhibitor, (b) superposition of the active site of the equilibrated structure (magenta carbon) and crystal structure (cyan carbon), (c) principal component analysis, (d) NCI plot of the S1′ site with amino acid residues labeled, (e) NCI plot of the S1 site with amino acid residues labeled, and (f) contact map of the S1 site.

of the **PSMA−In1** complex, although Lys699 is confirmed to clamp the terminal carboxylate group, the hydroxyl group of Tyr700 is approximately 5 Å away from the α-carboxylic group. The reason for this discrepancy could be that the strong $\pi-\pi$ interaction between Tyr700 and the aromatic ring of the P1 segment restricts the movement of this residue to a great extent.

The S1 pocket of PSMA exhibits the capability to accommodate various binding modes on the grounds of its high flexibility and accessory binding tunnel. The NCI contour plot of **PSMA−In1** in the S1 site (Figure 3e) illustrates that apart from coordinating to Zn2, the α-carboxylate group of **In1** forms a strong salt bridge (2.31 Å) with Arg536 and receives a strong hydrogen bond (1.70 Å) contributed by Tyr552. The phenyl ring of the P1 portion is sandwiched by two phenol rings of Tyr552 and Tyr700 through parallel-displaced $\pi-\pi$ stacking. The side chains of Arg210 and Tyr234 function like two gates to encompass the hydroxyl groups of boronic acid, exploiting the electrostatic and OH$-\pi$ interactions, respectively. Previous studies proposed that the aromatic ring of some inhibitors such as the PEGylated inhibitor[55] and DCIBzL[61] was trapped within an arginine patch (arginines 463, 534, and 536) and stabilized by cation$-\pi$ interactions. Normally, when PSMA was bound with natural substrate NAAG or in its resting state, the side chain of Arg536 was either in "stacking" or "binding" conformation, accompanied by the "up" or "down" position of the side chain of Arg463. The "binding" conformation of Arg536 was stabilized by the hydrogen bonds with the α-carboxylate group of P1. The opening of this patch or the so-called S1-accessory hydrophobic pocket was only associated with an abnormal combination of Arg463's "up" position and Arg536's "binding" conformation.[54,61] Although the full insertion of the terminal phenyl ring into the pocket led to the enhanced inhibition constant, this phenomenon was only observed for limited inhibitors with an appropriate length of the P1 chain and suitable substituent ligands (one halide atom on the para position of the phenyl ring). Nevertheless, it served as an important way to design and synthesize PSMA inhibitors with high binding affinity. However, in our simulation, even though Arg463 and Arg536 stay in an open state, **In1** rejects to enter this arginine patch. This is most likely due to the steric clash produced by the comparatively large boronic acid ligand with bifurcated hydroxyl groups. Instead, it is captured by another hydrophobic pocket (Figure S3a) surrounded by Arg210, Tyr234, Phe546, Tyr552, and Tyr700. Their intimate distances are also revealed by the contact map in Figure 3f. Therefore, the loss of binding affinity for not locating in the arginine patch is greatly compensated by the insertion of the P1 portion into another hydrophobic pitfall. The binding free energy of **In1** to PSMA is calculated to be −28.0 kcal/mol (Table 1), utilizing the λ particle approach in a thermodynamic cycle. This energy is mainly contributed by the following three interactions: (1) interactions between Zn ions and oxygen atoms of the inhibitor; (2) interactions between the S1′ site and the P1′ segment; 3. interactions between S1, especially the hydrophobic pocket, and the P1 region. Experimental results[67] on a structurally similar compound to **In1** demonstrated a half maximal inhibitory concentration (IC50) value of 130.3 nM, which was higher than that of 2-phosphonomethyl pentanedioic acid (strongest PSMA inhibitor ever reported, 2-PMPA, ∼0.3 nM)[71] but lower than that of glutamate (∼30 μM).[72]

https://doi.org/10.1021/acsomega.1c03554
ACS Omega 2021, 6, 33354−33369

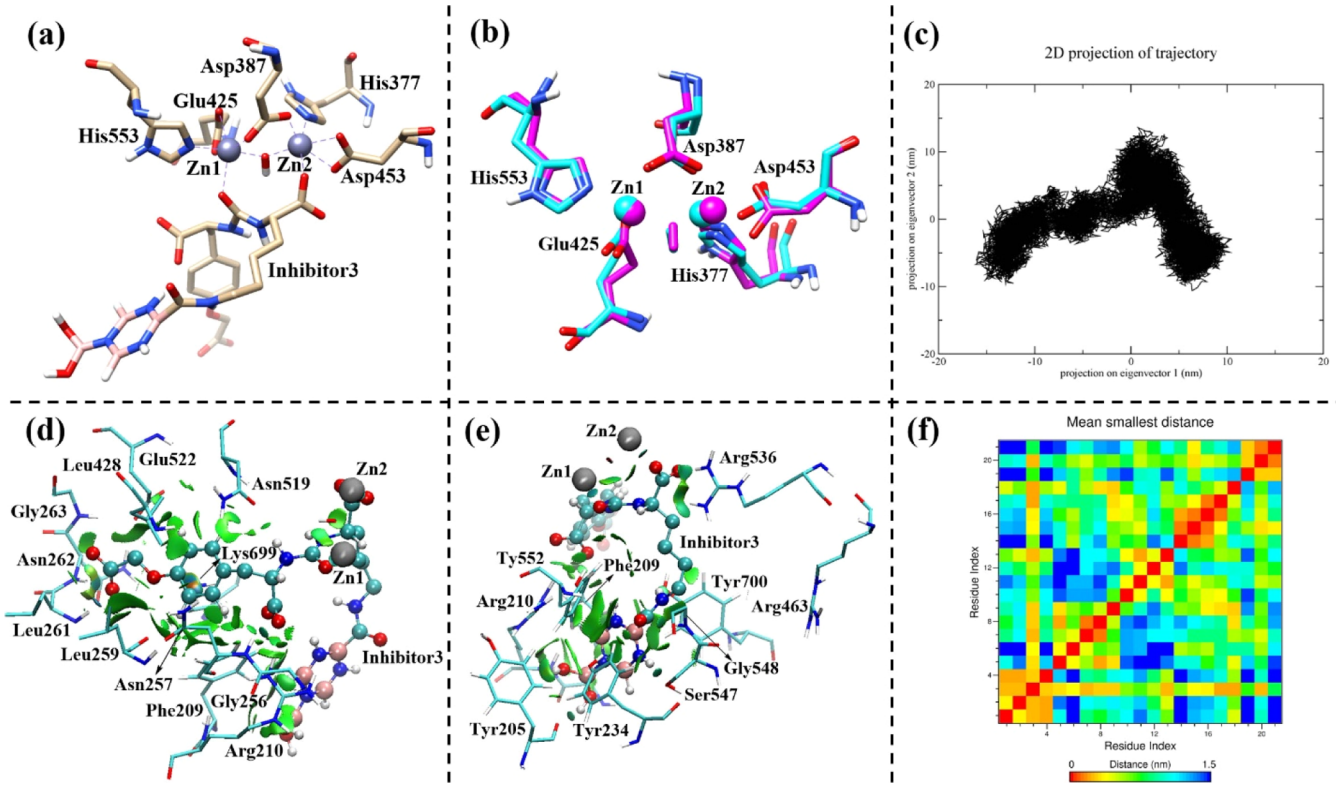

Figure 6. Most representative structure of the **PSMA−In3** complex derived from MD simulations: (a) active site with the inhibitor, (b) superposition of the active site of the equilibrated structure (magenta carbon) and crystal structure (cyan carbon), (c) principal component analysis, (d) NCI plot of the S1′ site with amino acid residues labeled, (e) NCI plot of the S1 site with amino acid residues labeled, and (f) contact map of the S1 site.

Although the IC50 value is not a direct indicator of binding affinity, the two can be related to each other using the Cheng−Prusoff equation.[73] Essentially, the lower the IC50 value, the higher the binding affinity and thus the more negative the binding free energy.

IIb. PSMA−In2 Interactions. A boronic ester—pinacolborane (4,4,5,5-tetramethyl-1,3,2-dioxaborolane shown in the circle in Figure 1) is attached to **In2** to investigate the influence of the ester group formed by bifurcated methyl groups. In contrast to **In1**, **In2** binds in the monodentate manner to the active site of PSMA (Figure 5a) that is characterized by the following factors: the ureido oxygen is engaged in the coordination of Zn1 (2.19 Å) and the P1 carboxylate group drifts away from the second metal Zn2 (4.67 Å). As a result, Zn2 coordinates to a previous second coordination shell residue—Glu424 (2.20 Å) to maintain its six coordination number and distorted octahedral geometry. Except for His377, all first coordination shell residues interact with both metal cations at a relatively longer distance in comparison to **PSMA−In1** (Table 1). On account of the large size of pinacolborane, the phenylboronic ester escapes from the hydrophobic site that wraps around **In1** and intercalates into the funnel-shaped tunnel that has enough space to accommodate large ligands. The equilibrated structure of the active site deviates from the crystal structure by an average of 1.41 Å (Figure 5b), winding up with significant displacement of nearly every residue and metal ion. Akin to **PSMA−In1**, the simulation of the **PSMA−In2** complex attains equilibrium at approximately 40 ns (Figures 3a and S1b). Upon **In2** binding, the population of conformational ensembles in **PSMA−In2** is quite comparable to that in **PSMA−In1** because the corresponding PCA (Figure 5c) reveals an R-shaped graph with a similar amount of energy basins and whole surface area.

The outline of the tunnel that incorporates the P1 part of **In2** is clearly observed in the NCI contour plot of the **PSMA−In2** complex (Figure S2b). In comparison to the **PSMA−In1** complex, the composition of the S1′ site is analogical but still composed of several different residues. The phenyl ring forms tilted T-shaped $\pi-\pi$ interaction with the side chain of Phe209. In contrast to **In1**, the terminal carboxylate group of **In2** forms only two hydrogen bonds (2.34 Å and 1.81 Å, respectively) with Leu261 and Asn262. Besides, this group and adjacent ester oxygen are recognized by the ε-amine group of Lys699 (N^{ζ}) through a weaker salt bridge (3.30 Å) and a weaker hydrogen bond (2.76 Å), respectively. All these differences may correlate with a slight rotation of P1′ in **PSMA−In2** induced by the position variance of P1. Analogous to **In1**, the strong $\pi-\pi$ interaction with the aromatic ring of P1 precludes Tyr700 to function as a "glutarate probe sensor". Alternatively, Asn257 takes the place of Tyr700 to interact with the α-carboxylate group of P1′, and Tyr700's contribution is largely compensated by π interactions around the aromatic ring of P1′.

Depicted in Figure 5e, the NCIs in the S1 site of the **PSMA−In2** complex are substantially weaker in comparison to **PSMA−In1**. The phenylboronic ligand breaks away from the clamp of Tyr552 and Tyr700, shifting to the accessory binding tunnel (Figure S3b) that contains sufficient space for its accommodation. In this tunnel, the side chain of Arg463 is included in a cation−π interaction with the phenyl ring of P1 and a hydrogen bonding with one ester oxygen atom. Parallel-displaced $\pi-\pi$ stacking manifests itself between the phenyl ring

https://doi.org/10.1021/acsomega.1c03554
ACS Omega 2021, 6, 33354−33369

and Tyr700. These interacting residues are clearly displayed as orange square points at the third row of the S1 site's contact map (Figure 5f). Since the size of boronic pinacol ester is larger than that of boronic acid, the possibility of its location at the preceding arginine patch can be completely obviated. The association of **In2** with PSMA demonstrates a subtly increased (1.7%) α-helix content (39.1%) but the overall similar secondary structure (Figure S4) as the **PSMA−In1** complex. The computed binding free energy for **In2** is −15.2 kcal/mol (Table 1), which is substantially higher than the one (−28.0 kcal/mol) calculated for **In1**. The decreased binding affinity of **In2** is substantiated by the increased IC50 value (318.4 nM) of an **In2** analogue[67] and is related to the conversion from the bidentate binding mode to the monodentate mode. The weaker NCIs in S1′ and S1 sites also contribute to this reduction.

IIc. PSMA−In3 Interactions. As discussed above, in order to invoke the successful BNCT, at least ∼20 μg of B^{10} per weight of tumor has to be selectively delivered into the tumor cells. Once these boron atoms absorb enough thermal neutrons, they will produce high LET α particles with pathlengths of 5−9 μm in tissues to destroy the boron-containing tumor cells while sparing the adjacent normal cells.[1,3] To achieve that, boron density should be enhanced by increasing the percentage of boron atoms within an inhibitor. In **In3**, the phenyl ring of P1 is substituted by a borazine ring, which is a cyclic compound constructed by three BH units and three NH units alternatively. Although isoelectronic and isostructural with benzene, borazine is suggested to be aromatic but possesses less electron delocalization than all-carbon analogues due to different electronegativities of the boron and nitrogen atoms.[74,75] **In3** coordinates to the bimetallic center of PSMA in a μ-1,6 bidentate fashion (Figure 6a) analogous to **In1**. The relative positions of the first coordination shell residues are preserved (Table 2) so that both Zn^{2+} ions are still six coordinated and adopt the distorted octahedral geometry. Based on the structural similarity, the boron ligand (borazine ring and boronic acid) of **In3** inserts into the same hydrophobic pocket that accommodates the phenylboronic acid of **In1**. The first and second principal components of α carbon atoms construct an inverse V-shaped graph in the PCA of the **PSMA−In3** complex (Figure 6c). In contrast to **PSMA−In1** and **PSMA−In2** complexes, fewer energy basins in this graph suggest that the **In3** binding triggers less structural variations in PSMA.

The overall microenvironment of **In3** inside PMSA resembles that of **In1** (Figure S2c). However, in comparison to **PSMA−In1**, Ser517 and Gly518 interchange their positions with Gly256 and Glu522 at the S1′ site of **PSMA−In3** (Figure 6d). The α-carboxylate group of P1′ in **In3** is recognized by the guanidinium moiety (N^{η}) of Arg210 and the backbone amino group of Asn257 through a salt bridge (2.43 Å) and a hydrogen bond (1.99 Å), respectively. The borazine ring of P1 approaches the side chains of Phe209 and Arg210, suggesting that **In3** intercalates more deeply into the S1′ site than **In1**. This deeper intercalation can also be confirmed by the shorter hydrogen bonds (1.74 and 1.92 Å) between the terminal carboxylate of P1′ and Leu261/Asn262. As a result, the aromatic ring in P1′ forms cation−π interactions with the ε-amine group of Lys699, while in the previous two cases, Lys699 interacts with the terminal carboxylate group through a salt bridge. Additionally, the phenyl ring of Phe209 further stabilizes the same aromatic ring by tilted T-shaped $\pi-\pi$ interactions. Similar to the complexes of **In1** and **In2**, Tyr552 and Tyr700 are restrained by the borazine ring of **In3**, preventing them from donating hydrogen bonds to the α-carboxylate group. On the other hand, the guanidinium group (N^{η}) of Arg536 in the S1 site (Figure 6e) interacts with the α-carboxylic group of P1 by a strong salt bridge (2.16 Å), thus staying in the "binding" conformation. Arg463 can play the role of position mark, and the absence of its interaction with **In3** indicates that the inhibitor is engaged in a translational motion toward the S1′ site and the boron ligand is more buried in the hydrophobic pocket (Figure S3c). In the **PSMA−In1** complex, the aromatic ring of P1 interacts with Tyr552 and Tyr700, while Arg210 and Tyr234 only form interactions with the hydroxyl groups of boronic acid. In contrast, albeit with a slightly weaker aromaticity, the increased localization of electrons on the BH and NH units of the borazine ring can interact with Arg210 and Tyr234. Moreover, it turns out that all these four residues and Phe209 besiege the borazine ring (close distances shown in Figure 6f). The phenyl ring of Phe209 and the phenol rings of Tyr552/Tyr700 form $\pi-\pi$ interactions with the borazine ring, which in turn associates with Tyr234 through OH−π interaction. A binding free energy of −43.9 kcal/mol for **In3** is significantly lower than those for **In1** and **In2** (Table 2). This difference suggests that PSMA prefers to associate with **In3**. The stronger binding of **In3** than of **In2** is understandable (bidentate vs monodentate binding). However, its stronger binding in comparison to **In1** is trivial. From the viewpoint of NCIs, the slightly less aromatic but more electrostatic borazine ring of **In3** is more buried in the hydrophobic pocket, producing more interactions around the boron ligand and pushing P1′ more deeply into the S1′ site. This movement again generates more $\pi-\pi$ interactions around the phenyl ring of P1′ and stronger hydrogen bonds on the terminal carboxylate group.

Table 2. Metal Coordination Number and Metal−Metal, Metal−Substrate, Metal−OH, and Metal−Ligand Distances (Å) for the First Coordination Shell Residues in PSMA Equilibrated Structures (Inhibitors 3, 4, and 5) and the Calculated Binding Free Energies of Distinct Inhibitors (kcal/mol)[a]

	PSMA−In3	PSMA−In4	PSMA−In5
coordination number	6(Zn1), 6(Zn2)	7(Zn1), 6(Zn2)	7(Zn1), 6(Zn2)
$M_{Zn1}-M_{Zn2}$	3.48	3.40	3.35
inhibitor	2.24(Zn1), 2.24(Zn2)	2.18,2.43(Zn1), 2.32(Zn2)	2.20, 2.50(Zn1), 2.36(Zn2)
μOH	1.89(Zn1), 1.85(Zn2)	1.85(Zn1), 1.87(Zn2)	1.87(Zn1), 1.99(Zn2)
His377	2.15(Zn2)	2.07(Zn2)	1.96(Zn2)
Asp387	2.26(Zn1), 2.11(Zn2)	2.09(Zn1), 2.12(Zn2)	2.39(Zn1), 2.05(Zn2)
Glu424	8.52(Zn2)	6.00(Zn2)	4.48(Zn2)
Glu425	2.25, 2.11(Zn1)	2.27, 2.11(Zn1)	2.20, 2.27(Zn1)
Asp453	2.11, 2.17(Zn2)	2.27, 2.17(Zn2)	2.12, 2.24(Zn2)
His553	2.15(Zn1)	2.05(Zn1)	2.02(Zn1)
binding free energy	−43.9	−23.2	−38.2

[a]Metal coordination sites (Zn1 and Zn2) are shown in the parentheses.

https://doi.org/10.1021/acsomega.1c03554
ACS Omega 2021, 6, 33354−33369

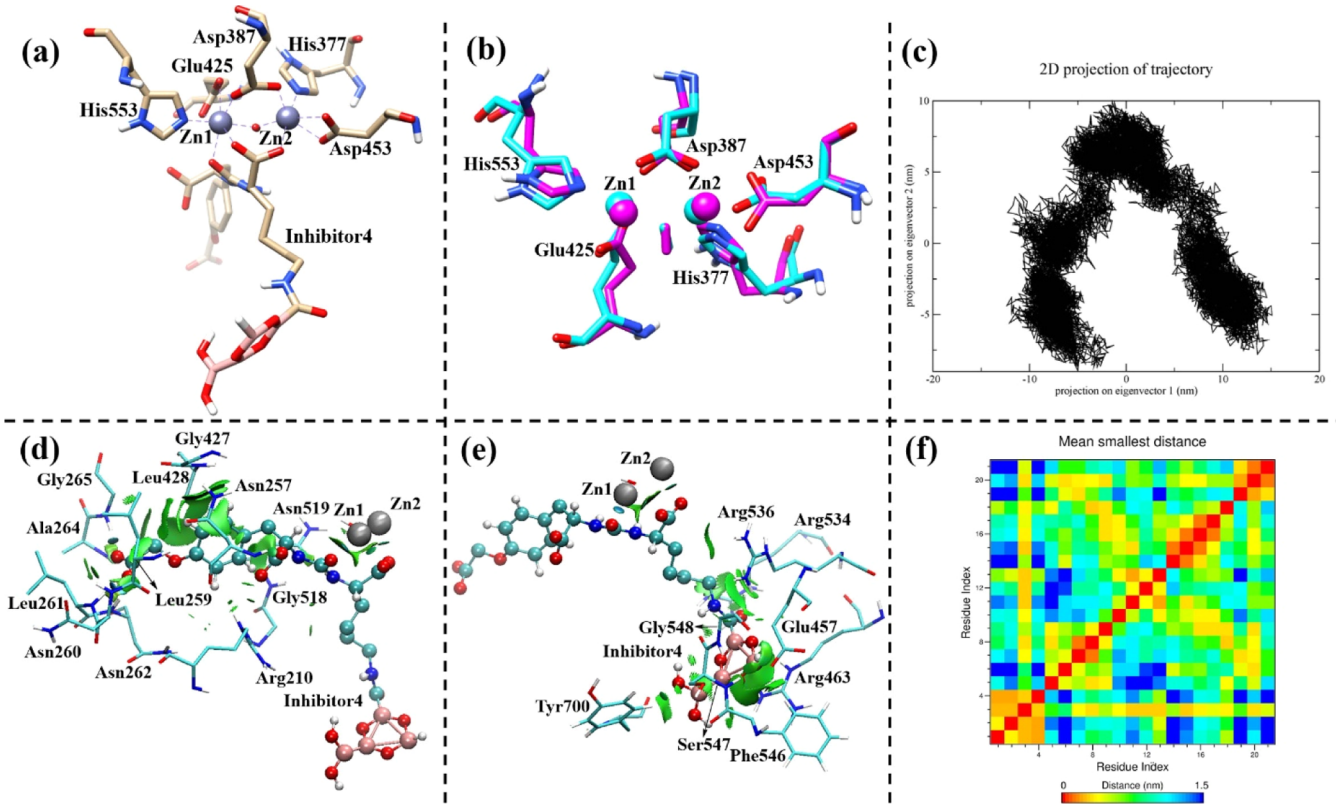

Figure 7. Most representative structure of the **PSMA−In4** complex derived from MD simulations: (a) active site with the inhibitor, (b) superposition of the active site of the equilibrated structure (magenta carbon) and crystal structure (cyan carbon), (c) principal component analysis, (d) NCI plot of the S1′ site with amino acid residues labeled, (e) NCI plot of the S1 site with amino acid residues labeled, and (f) contact map of the S1 site.

IId. PSMA−In4 Interactions. **In4** consists of the same number of boron atoms as **In3**, but it contains a different aromatic ring—boroxine ring, which is composed of alternating oxygen and singly hydrogenated boron atoms (shown in the circle in Figure 1). Thus, the boronic acid can only occupy the meta rather than the para position with respect to the P1 chain. The boroxine is also isoelectronic to benzene, yet it possesses less aromatic character than borazine due to the larger difference in electronegativity between the oxygen and boron atoms.[76] With vacant p-orbitals on boron atoms, boroxine can accept electrons from phenyl or negatively charged groups. In the active site of **PSMA−In4** (Figure 7a), all three oxygens from the ureido linkage and carboxylate side chain of P1 are involved in a tripartite ligation of the bimetallic cations. This appealing observation seems to be a bit gratuitous at first glance but maybe correlated with the movement of the P1 part in the S1 site. Although the coordination between the carboxylate oxygen and Zn1 is loose (2.43 Å, Table 2), it alters the molecular geometry at the Zn1 site from the distorted octahedron to the distorted pentagonal bipyramid. First coordination shell residues experienced some fluctuations (Figure 4b) and display a slightly higher RMSD value (0.76 Å, Figure 7b) than those for **In1** and **In3** complexes. The PCA of the **PSMA−In4** complex (Figure 7c) offers an inverse V-shaped graph that has four distinct energy basins. Since PCA of the **In3** complex has a similar number of energy basins, these two inhibitors are considered to generate comparable conformations during the simulations.

As expected, the meta substitution of boronic acid on the boroxine ring causes it to jump out of the hydrophobic pocket that can occupy both **In1** and **In3**. The drift of the boron ligand of **In4** is deemed to result in the tripartite coordination to the bimetallic site and the shift-up of the P1′ part, which promotes the loss of contact between P1′ and Phe209/Lys699 (Figures 7d and S2d). Additionally, the salt bridge between Arg210 and the α-carboxylate side chain of P1′ becomes very weak (3.04 Å), while the hydrogen bond (2.28 Å) donated from Asn257 is conserved. The residues of Asn257, Gly427, Leu428, and Asn519 contribute to the stabilization of the phenyl ring of P1′from both the sides. Furthermore, the terminal carboxylate group is trapped by a hydrogen bonding network created by residues Leu261, Asn262, Ala264, and Gly265. In the S1 site, the boron ligand resides itself in the accessory binding tunnel (Figure S3d) and less NCIs are observed between **In4** and environmental residues (Figure 7e,f). The α-carboxylate group of P1 makes a very weak salt bridge (4.00 Å) with the guanidinium moiety (N^{η}) of Arg536. Differing from previously inhibitors, Arg534 also exhibits some weak electrostatic interactions with the amide bond of P1. A nearly perfect cation−π interaction manifests itself between the boroxine ring and the guanidinium group of Arg463. It is noteworthy that the boroxine ring is completely devoid of $\pi-\pi$ interaction with Tyr700 due to its' weaker aromaticity. In general, tripartite ligation of the inhibitor to metal ions is suggestive of a high binding potency. Nevertheless, the binding free energy of **In4** is computed to be −23.2 kcal/mol, which is 4.8 and 20.7 kcal/mol higher than those of **In1** and **In3**, respectively. This lower binding affinity could be explained by less NCIs around the boron ligand, weaker salt bridges on α-

https://doi.org/10.1021/acsomega.1c03554
ACS Omega 2021, 6, 33354−33369

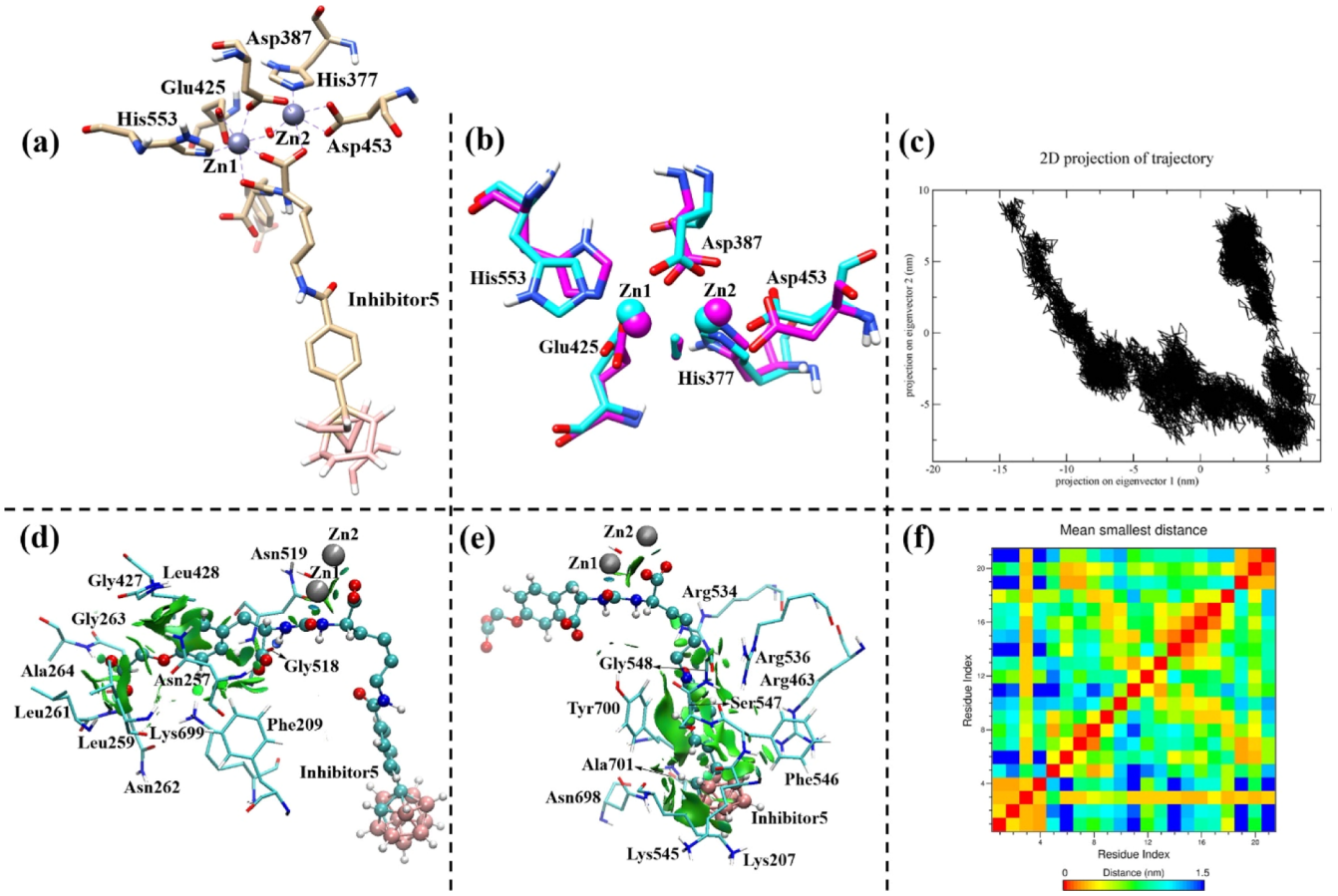

Figure 8. Most representative structure of the **PSMA−In5** complex derived from MD simulations: (a) active site with the inhibitor, (b) superposition of the active site of the equilibrated structure (magenta carbon) and crystal structure (cyan carbon), (c) principal component analysis, (d) NCI plot of the S1′ site with amino acid residues labeled, (e) NCI plot of the S1 site with amino acid residues labeled, and (f) contact map of the S1 site.

carboxylate groups, and loss of contact with Phe209/Lys699 described previously.

IIe. PSMA−In5 Interactions. In order to further increase the boron density within PSMA, a *closo* carborane ball (1,2-$C_2B_{10}H_{11}^{-1}$, shown in the circle in Figure 1) is attached to the phenyl ring of P1 to create **In5**. 1,2-$C_2B_{10}H_{11}^{-1}$ is an icosahedral electron-delocalized nonclassical bonding cluster composed of hydrogen, boron, and carbon atoms.[77] It is usually characterized by the electron-deficient 3-center 2-electron (3c-2e) chemical bond, and its stability is derived from completely filled bonding molecular orbitals. The carborane clusters and related metallacarboranes are employed in a wide range of applications including catalysis, medicines, electroactive materials, and recovery of radioactive metals from nuclear waste and heat-resistant polymers. The electronic structures of these electron-delocalized polyhedral compounds can be predicted by the Wade-Mingos rules[78,79] that are invoked depending on the number of electrons per vertex. The equilibrated structure of the **PSMA−In5** active site (Figure 8a) displays a tripartite coordination similar to that of the **PSMA−In4** complex. The comparatively large-sized carborane ball is completely accommodated in the accessory binding tunnel like the cases of **In2** and **In4**. This is in accordance with the crystal structure of PSMA in complex with a carborane-containing inhibitor.[60] Large deviations in the equilibrated active site of **PSMA−In5** are reflected by the high RMSD value (1.38 Å, Figure 8b). When compared with **In1−In4**, the conformational variations upon binding of **In5** are the largest because the PCA of the **PSMA−In5** complex (Figure 8c) shows a unique U-shaped plot with maximum conformational ensembles. It illustrates that the accommodation of **In5** inside PSMA induces maximum structural variations in contrast to all previous inhibitors.

Just like the **In2** complex, the shape of the accessory binding tunnel is clearly shown in the NCI plot of the whole cavity in **PSMA−In5** (Figure S2e). Due to similar positions of the boron ligand and identical tripartite ligation, the P1′ part of **In5** resembles that of **In4** in terms of the NCIs in the S1′ site. The absence of salt bridges contributed by Arg210 and Lys699 could be ascribed to the upward movement of the P1′ portion. The β-amide group of Asn257 and the peptide bond of Gly427/Leu428 are involved in parallel and tilted T-shaped π stacking with the aromatic ring of P1′, respectively. The methylene/methyl groups of Leu428 engaged in CH−π interactions with the same ring, which adopts a tilted T-shaped arrangement relative to the side chain of Phe209. It is worth mentioning that aromatic-amide interaction is one of the most common NCIs in proteins. However, the NH−π contacts are generally outnumbered by the aromatic-amide-stacked structures with the sp^2-hybridized nitrogen atoms.[80] This phenomenon can be attributed to the higher number of conventional hydrogen bonds the NH group can form in the stacked orientation.[81] Analogously, the terminal carboxylate side chain interacts with the backbone amino groups of

https://doi.org/10.1021/acsomega.1c03554
ACS Omega 2021, 6, 33354−33369

Leu261, Asn262, Gly263, and Ala264 via hydrogen bonds. In the accessory binding tunnel (Figure S3e), the P1 of **In5** displays more interactions with residues that wrap around it (Figure 8e) in comparison to **In2** and **In4**. Two strong hydrogen bonds (2.07 and 2.32 Å) are formed between the carbonyl oxygen of amide in P1 and guanidinium protons (H^{θ}) of Arg534. The aromatic ring of P1 is arranged in a perfect parallel-displaced π stacking with the phenol ring of Tyr700 on one side. On the other hand, the backbone carbonyl bond, α-methylene group, and phenyl ring of Phe546 add to the stability of this aromatic ring. Being electron-deficient, the carborane ball is predisposed to receive electrons from electron-donating groups to enhance the delocalization effect. The methylene groups of Lys207, guanidinium group of Arg463, peptide bond of Lys545/Phe546, γ-amino group of Asn698, backbone carbonyl oxygen of Tyr700, and α-methyl group of Ala701 are all found to donate electrons to carborane. All these interactions and tripartite coordination are confirmed in the contact map (Figure 8f), thus predicting a high binding potency for **In5**. Its binding free energy is calculated to be −38.2 kcal/mol, which is the second lowest among all inhibitors studied. This may result from the lack of three salt bridges that originated from Arg210, Lys699, and Arg536 in the **PSMA−In5** complex. The IC50 value of an **In5** mimic was measured to be 20.3 nM.[67] Moreover, a series of *closo-*, *nido-*, and iodo-C-hydroxy carborane clusters have been reported to bind with PSMA for BNCT.[66] Among them, a radiolabeled ^{123}I analogue exhibited the highest affinity with an IC50 value of 73.2 nM. This indicated that except for the urea-based scaffold, the carborane cluster is also tolerant with respect to structural modification. In this situation, it is beneficial for us to search for the best BNCT compounds by modifying the existing molecules.

III. SUMMARY AND CONCLUSIONS

In this study, the molecular docking and MD simulation techniques have been employed to investigate the binding potencies and interactions of five potential urea-based boron-containing inhibitors with PSMA. These inhibitors are derived from the common urea-based PSMA binding skeleton that has been reported previously. They contain chemically distinct boron ligands (Figure 1): (1) phenylboronic acid in **In1**; (2) phenylboronic ester in **In2**; (3) borazine ring and boronic acid in **In3**; (4) boroxine ring and boronic acid in **In4**; and (5) carborane ball in **In5**. The number of boron atoms within one molecule is gradually increased from 1 to 10 because the effective BNCT not only requires the strong binding affinity of the inhibitor to the target protein but also necessitates the high boron density within tumor cells.[3,5] It is found that different inhibitors bind in a rather distinct mode to generate PSMA−inhibitor complexes, which are mainly dominated by hydrogen bonding, salt bridge, electrostatic, and $\pi-\pi$ interactions. Specifically, **In1** and **In3** bind to the bimetallic active site in a μ-1,6 bidentate mode. Their boron ligands are inserted into a hydrophobic pocket encompassed by Arg210, Tyr234, Tyr552, and Tyr700 (Figure S3). In contrast, **In2** is singly coordinated to Zn1, while **In4** and **In5** are involved in a tripartite ligation to both metal ions. The boron ligands of these three inhibitors are accommodated in the funnel-shaped tunnel due to different reasons: the comparatively large size of boron ligands in **In2** and **In5** and the meta substitution of boronic acid on the boroxine ring in **In4**. Nonetheless, they all share a commonality: none of the ligands are trapped in the arginine patch mentioned in the previous studies.[55,61] This may be attributed to the steric hindrance created by those large boron ligands. By and large, these results demonstrate the flexibility of the S1 site of PSMA because the P1 portion of an inhibitor can be located in various positions based on its chemical nature. On the other hand, the P1′ part of all inhibitors is located in the S1′ site of PSMA and interactions around this part are influenced by the position of the P1 portion. For **In3**, the P1′ intercalates deeper into the S1′ site, exhibiting more interactions with PSMA. However, for **In4** and **In5**, the P1′ shifts up and loses contact with several important residues (Phe209 and Lys699) at the bottom of the S1′ site.

The association of the inhibitor to PSMA does not alter the overall secondary structure of PSMA (Figures S4 and S5), which consists of approximately 38% helical and 15% beta-sheet conformations. The binding free energies are calculated using the λ-particle approach in a thermodynamic cycle and are analyzed based on the NCIs between the inhibitor and PSMA. The computed free energies suggest a binding preferential order (Tables 1 and 2): **In3** (−43.9 kcal/mol) > **In5** (−38.2 kcal/mol) > **In1** (−28.0 kcal/mol) > **In4** (−23.2 kcal/mol) > **In2** (−15.2 kcal/mol). The measured IC50 values (130.3, 318.4, and 20.3 nM)[67] for analogues of three inhibitors (**In1**, **In2**, and **In5**) are in excellent agreement with the order predicted by binding free energies. Even though the binding property of **In3** to PSMA is the best, the boron density of **In5** is the highest and its binding potency is only slightly lower than that of **In3**. By taking into account the balance between binding potency and boron density, **In5** should be considered as the best option for BNCT. In summary, our computational study can complement experimental binding studies between PSMA and potential BNCT reagents that are typically performed by isothermal calorimetry (ITC) or Trp fluorescence spectroscopy. It provides the detailed atomistic and thermodynamic properties of each enzyme−inhibitor complex that may be useful for the design of **In5** like PSMA inhibitors. This information is expected to stimulate the development of effective PSMA-targeted BNCT reagents with both high boron density and enhanced binding affinity. However, they need to be synthesized and characterized using experimental techniques.

IV. COMPUTATIONAL DETAILS

The 1.84 Å resolution crystal structure of PSMA (PDB ID: 4NGM) was obtained from Protein Data Bank (PDB).[55] The structures of various urea-based boron-containing inhibitors were fully optimized without any geometrical constraint at the B3LYP[82]/6-31G(d)[83] theory level by utilizing the Gaussian 09 program.[84] These optimized structures were used to develop their force field parameters utilizing Automated Topology Builder (ATB).[85] These parameters are compatible with the GROMOS force field family in a wide range of formats. The molecular docking procedure was performed using Autodock Vina 1.5.6 software[86] to derive the binding poses of inhibitors to the bimetallic active site of PSMA. Two docking approaches (rigid docking and flexible docking) were used to yield 20 poses with an exhaustiveness value of 20 for each trial, and the size of the grid box was chosen to cover the entire active site of PSMA. The lowest energy poses provided by these docking protocols were used as the starting points for MD simulations, which were performed using the GROMACS program[87] and the Gromos 54A7 force field.[88] The enzyme−substrate complexes were equilibrated in a cubic box with dimensions

https://doi.org/10.1021/acsomega.1c03554
ACS Omega 2021, 6, 33354−33369

of 10 × 10 × 10 nm for all simulations to obviate the adverse impacts that maybe induced by the application of periodic boundary conditions.[89] This box was saturated with SPC water molecules,[90] some of which were replaced by sodium and chloride ions to simulate a physiological ion concentration of 154 mM and neutralize the system. Since the active site of PMSA is deeply buried away from the water solvent, SPC is an adequate water model for this system. The energy minimization with 3000 steps was performed on the starting structures through the steepest descent method with the coordinates of the active site and inhibitor frozen. The resulting structures from that energy minimization were first equilibrated for 20 ns by placing distance restraints around the active site and substrate to minimize the energy of the environment. Subsequently, the MD simulations on these equilibrated structures were performed for 100 ns without any restraints. All these simulations were carried out using a constant number of particles (N), pressure (P), and temperature (T), that is, NPT ensemble or isobaric ensemble. The LINCS algorithm[91] was employed to constrain the bond lengths of the peptide, and the SETTLE algorithm[92] was used to constrain the bond lengths and angles of water molecules. The long-range electrostatic interactions were calculated using the particle mesh Ewald (PME) method[93] with a cutoff value of 1.2 nm. Peptides, metal ions, inhibitors, water molecules, and ions were coupled separately in a bath at 1 atm and 300 K with coupling constants of 1.0 and 0.1 ps, respectively. A time step of 2 fs was utilized to compute the trajectory of each model, and a pH of 7.0 was used to set amino acid residues to their normal ionization states.

Several built-in tools within GROMACS were employed to analyze the trajectories obtained from MD simulations. The most representative structures of enzyme−substrate complexes were derived from the cluster analysis, in which the frame with the greatest number of neighbors was selected as the middle structure to represent the cluster that has been constructed by grouping together the structurally similar frames (RMSD cutoff of 0.3 nm). The computed RMSD and pairwise RMSD[94] values confirmed the convergence of all equilibrated structures within the simulation timeframe. The binding free energies between PSMA and inhibitors were calculated by the lambda (λ) particle approach[95−97] in a thermodynamic cycle that describes the bound and unbound states. In this cycle, the relative binding energies between an enzyme and a ligand can be defined as the difference in free energy associated with the chemical changes of the ligand into the enzyme in their bound and solvated states. In this approach, the Coulombic and van der Waals interactions between PSMA and inhibitors were turned off in a sequential and systematic way: first Coulombic interactions were turned off and then the van der Waals interactions. This sequence of operations avoided the interactions of opposite charges at intimate distances, which could lead to unrealistic configurations and imprecise energies. The soft-core interactions[98] were applied to Lennard-Jones and Coulomb potentials to remove singularities in these potentials and circumvent a poor convergence at λ close to 0 or 1. The values of soft-core parameters (α, sc_alpha in mdp), soft-core power (λ, sc_power in mdp), and radius of interaction (σ, sc_sigma in mdp) when either C6 or C12 is zero were set to 0.5, 1.0, and 0.3, respectively. NCIs between inhibitors and PSMA were calculated and visualized using the NCIPLOT program,[99] which identifies the NCIs based on the electron densities and their derivatives. The contact maps and defined secondary structure protocol (DSSP)[100] of all complexes were generated from their compacted trajectory files (xtc files) by inbuilt tools of mdmat and DSSP within the GROMACS software package. The zinc metal ions, inhibitors, and S1 site residues were chosen as references to highlight their relative positions in the contact maps. They were labeled by the residue index in a numerical order as listed below: 1-Zn1, 2-Zn2, 3-inhibitor, 4-μOH, 5-Tyr205, 6-Lys207, 7-Phe209, 8-Arg210, 9-Tyr234, 10-Glu457, 11-Arg463, 12-Arg534, 13-Arg536, 14-Lys545, 15-Phe546, 16-Ser547, 17-Gly548, 18-Tyr552, 19-Asn698, 20-Tyr700, and 21-Ala701. ESP of PSMA was created using Adaptive Poisson-Boltzmann Solver software[101] and visualized with PyMol.[102] In addition, VMD,[103] ChemDraw,[104] YARASA,[105] and Chimera[106] software programs were also utilized to visualize and prepare the diagrams used in this study. The conformational dynamics of all complexes were investigated by performing principal component analysis (PCA)[107,108] of the alpha carbon atoms. The PCA reduces the dimensionality of large data variables, while preserving as much information as possible.

■ ASSOCIATED CONTENT

Supporting Information

The Supporting Information is available free of charge at https://pubs.acs.org/doi/10.1021/acsomega.1c03554.

Pairwise RMSD of all complexes; NCI plots of the whole cavity of all complexes; accessory binding pocket/tunnel in the S1 site of all complexes; and DSSP (PDF)

■ AUTHOR INFORMATION

Corresponding Authors

Rajeev Prabhakar − *Department of Chemistry, University of Miami, Coral Gables, Florida 33146, United States;* orcid.org/0000-0003-1137-1272; Phone: 305-284-9372; Email: rpr@miami.edu; Fax: 305-284-4571

Wensi Tao − *Department of Radiation Oncology, University of Miami Miller School of Medicine, Miami, Florida 33136, United States;* orcid.org/0000-0003-2396-9829; Phone: 305-607-8266; Email: wtao@med.miami.edu

Authors

Qiaoyu Hu − *Department of Chemistry, University of Miami, Coral Gables, Florida 33146, United States*

Kevin Padron − *Department of Computer Science, University of Miami, Coral Gables, Florida 33146, United States*

Daiki Hara − *Department of Radiation Oncology, University of Miami Miller School of Medicine, Miami, Florida 33136, United States*

Junwei Shi − *Department of Radiation Oncology, University of Miami Miller School of Medicine, Miami, Florida 33136, United States*

Alan Pollack − *Department of Radiation Oncology, University of Miami Miller School of Medicine, Miami, Florida 33136, United States*

Complete contact information is available at: https://pubs.acs.org/10.1021/acsomega.1c03554

Author Contributions

The manuscript was written through contributions of all authors.

https://doi.org/10.1021/acsomega.1c03554
ACS Omega 2021, 6, 33354−33369

Funding

This material is based upon work supported by the grant of the National Science Foundation (Grant Number CHE-1664926) to R.P. and SCCC American Cancer Society (IRG) pilot project grants to W.T.

Notes

The authors declare no competing financial interest.

■ ACKNOWLEDGMENTS

Computational resources from the Institute for Data Science and Computing (IDSC) at the University of Miami are greatly appreciated.

■ ABBREVIATIONS

PSMA, prostate-specific membrane antigen; MD, molecular dynamics; RMSD, root-mean-square deviations; BNCT, boron neutron capture therapy; In1, Inhibitor1; In2, Inhibitor2; In3, Inhibitor3; In4, Inhibitor4; In5, Inhibitor5; LET, linear energy transfer; GCPII, glutamate carboxypeptidase II; *FOLH1*, folate hydrolase 1; NAAG, *N*-acetyl-L-aspartyl-L-glutamate; NAA, *N*-acetylaspartate; PDB, Protein Data Bank; ATB, Automated Topology Builder; PME, particle mesh Ewald; NCIs, non-covalent interactions; DSSP, defined secondary structure protocol; ESP, electrostatic surface potential; PCA, principal component analysis; SAR, structure−activity relationship; GpdQ, glycerolphosphodiesterase; IC50, half maximal inhibitory concentration; 2-PMPA, 2-phosphonomethyl pentanedioic acid; ITC, isothermal calorimetry

■ REFERENCES

(1) Barth, R. F.; Coderre, J. A.; Vicente, M. G. H.; Blue, T. E. Boron Neutron Capture Therapy of Cancer: Current Status and Future Prospects. *Clin. Cancer Res.* **2005**, *11*, 3987−4002.

(2) Moss, R. L. Critical Review, with an Optimistic Outlook, on Boron Neutron Capture Therapy (BNCT). *Appl. Radiat. Isot.* **2014**, *88*, 2−11.

(3) Barth, R. F.; Mi, P.; Yang, W. Boron Delivery Agents for Neutron Capture Therapy of Cancer. *Cancer Commun.* **2018**, *38*, 35.

(4) Hopewell, J. W.; Morris, G. M.; Schwint, A.; Coderre, J. A. The Radiobiological Principles of Boron Neutron Capture Therapy: A Critical Review. *Appl. Radiat. Isot.* **2011**, *69*, 1756−1759.

(5) Soloway, A. H.; Tjarks, W.; Barnum, B. A.; Rong, F.-G.; Barth, R. F.; Codogni, I. M.; Wilson, J. G. The Chemistry of Neutron Capture Therapy. *Chem. Rev.* **1998**, *98*, 1515−1562.

(6) Barth, R. F.; Vicente, M. G.; Harling, O. K.; Kiger, W., 3rd; Riley, K. J.; Binns, P. J.; Wagner, F. M.; Suzuki, M.; Aihara, T.; Kato, I.; Kawabata, S. Current Status of Boron Neutron Capture Therapy of High Grade Gliomas and Recurrent Head and Neck Cancer. *Radiat. Oncol.* **2012**, *7*, 146.

(7) Soloway, A. H.; Hatanaka, H.; Davis, M. A. Penetration of Brain and Brain Tumor. VII. Tumor-binding Sulfhydryl Boron Compounds. *J. Med. Chem.* **1967**, *10*, 714−717.

(8) Mishima, Y.; Honda, C.; Ichihashi, M.; Obara, H.; Hiratsuka, J.; Fukuda, H.; Karashima, H.; Kobayashi, T.; Kanda, K.; Yoshino, K. Treatment of Malignant Melanoma by Single Thermal Neutron Capture Therapy with Melanoma-seeking 10B-compound. *Lancet* **1989**, *334*, 388−389.

(9) Mishima, Y.; Ichihashi, M.; Hatta, S.; Honda, C.; Sasase, A.; Yamamura, K.; Kanda, K.; Kobayashi, T.; Fukuda, H. Selective Thermal Neutron Capture Therapy and Diagnosis of Malignant Melanoma: from Basic Studies to First Clinical Treatment. *Basic Life Sci.* **1989**, *50*, 251−260.

(10) Wittig, A.; Huiskamp, R.; Moss, R. L.; Bet, P.; Kriegeskotte, C.; Scherag, A.; Hilken, G.; Sauerwein, W. A. G. Biodistribution of (10)B for Boron Neutron Capture Therapy (BNCT) in a Mouse Model After Injection of Sodium Mercaptoundecahydro-closo-dodecaborate and l-para-boronophenylalanine. *Radiat. Res.* **2009**, *172*, 493−499.

(11) Miyatake, S.-I.; Kawabata, S.; Kajimoto, Y.; Aoki, A.; Yokoyama, K.; Yamada, M.; Kuroiwa, T.; Tsuji, M.; Imahori, Y.; Kirihata, M.; Sakurai, Y.; Masunaga, S.-I.; Nagata, K.; Maruhashi, A.; Ono, K. Modified Boron Neutron Capture Therapy for Malignant Gliomas Performed Using Epithermal Neutron and Two Boron Compounds with Different Accumulation Mechanisms: An Efficacy Study Based on Findings on Neuroimages. *J. Neurosurg.* **2005**, *103*, 1000−1009.

(12) Kawabata, S.; Miyatake, S.; Nonoguchi, N.; Hiramatsu, R.; Iida, K.; Miyata, S.; Yokoyama, K.; Doi, A.; Kuroda, Y.; Kuroiwa, T.; Michiue, H.; Kumada, H.; Kirihata, M.; Imahori, Y.; Maruhashi, A.; Sakurai, Y.; Suzuki, M.; Masunaga, S.; Ono, K. Survival Benefit from Boron Neutron Capture Therapy for the Newly Diagnosed Glioblastoma Patients. *Appl. Radiat. Isot.* **2009**, *67*, S15−S18.

(13) Miyatake, S.; Kawabata, S.; Yokoyama, K.; Kuroiwa, T.; Michiue, H.; Sakurai, Y.; Kumada, H.; Suzuki, M.; Maruhashi, A.; Kirihata, M.; Onoc, K. Survival Benefit of Boron Neutron Capture Therapy for Recurrent Malignant Gliomas. *Appl. Radiat. Isot.* **2009**, *67*, S22−S244.

(14) Kankaanranta, L.; Saarilahti, K.; Mäkitie, A.; Välimäki, P.; Tenhunen, M.; Joensuu, H. Boron Neutron Capture Therapy (BNCT) Followed by Intensity Modulated Chemoradiotherapy as Primary Treatment of Large Head and Neck Cancer with Intracranial Involvement. *Radiother. Oncol.* **2011**, *99*, 98−99.

(15) Barth, R. F.; Zhang, Z.; Liu, T. A Realistic Appraisal of Boron Neutron Capture Therapy as a Cancer Treatment Modality. *Cancer Commun.* **2018**, *38*, 36.

(16) Kabalka, G. W.; Yao, M. L.; Marepally, S. R.; Chandra, S. Biological Evaluation of Boronated Unnatural Amino Acids as New Boron Carriers. *Appl. Radiat. Isot.* **2009**, *67*, S374−S379.

(17) Barth, R. F.; Kabalka, G. W.; Yang, W.; Huo, T.; Nakkula, R. J.; Shaikh, A. L.; Haider, S. A.; Chandra, S. Evaluation of Unnatural Cyclic Amino Acids as Boron Delivery Agents for Treatment of Melanomas and Gliomas. *Appl. Radiat. Isot.* **2014**, *88*, 38−42.

(18) Yanagië, H.; Ogata, A.; Sugiyama, H.; Eriguchi, M.; Takamoto, S.; Takahashi, H. Application of Drug Delivery System to Boron Neutron Capture Therapy for Cancer. *Expert Opin. Drug Delivery* **2008**, *5*, 427−443.

(19) Backer, M. V.; Gaynutdinov, T. I.; Patel, V.; Bandyopadhyaya, A. K.; Thirumamagal, B. T. S.; Tjarks, W.; Barth, R. F.; Claffey, K.; Backer, J. M. Vascular Endothelial Growth Factor Selectively Targets Boronated Dendrimers to Tumor Vasculature. *Mol. Cancer Ther.* **2005**, *4*, 1423−1429.

(20) Yang, W.; Wu, G.; Barth, R. F.; Swindall, M. R.; Bandyopadhyaya, A. K.; Tjarks, W.; Tordoff, K.; Moeschberger, M.; Sferra, T. J.; Binns, P. J.; Riley, K. J.; Ciesielski, M. J.; Fenstermaker, R. A.; Wikstrand, C. J. Molecular Targeting and Treatment of Composite EGFR and EGFRvIII-positive Gliomas Using Boronated Monoclonal Antibodies. *Clin. Cancer Res.* **2008**, *14*, 883−891.

(21) Yang, W.; Barth, R. F.; Wu, G.; Kawabata, S.; Sferra, T. J.; Bandyopadhyaya, A. K.; Tjarks, W.; Ferketich, A. K.; Moeschberger, M. L.; Binns, P. J.; Riley, K. J.; Coderre, J. A.; Ciesielski, M. J.; Fenstermaker, R. A.; Wikstrand, C. J. Molecular Targeting and Treatment of EGFRvIII-positive Gliomas Using Boronated Monoclonal Antibody L8A4. *Clin. Cancer Res.* **2006**, *12*, 3792−3802.

(22) Barth, R. F.; Yang, W.; Wu, G.; Swindall, M.; Byun, Y.; Narayanasamy, S.; Tjarks, W.; Tordoff, K.; Moeschberger, M. L.; Eriksson, S.; Binns, P. J.; Riley, K. J. Thymidine Kinase 1 as a Molecular Target for Boron Neutron Capture Therapy of Brain Tumors. *Proc. Natl. Acad. Sci. U.S.A.* **2008**, *105*, 17493−17497.

(23) Doble, A. The Role of Excitotoxicity in Neurodegenerative Disease: Implications for Therapy. *Pharmacol. Ther.* **1999**, *81*, 163−221.

(24) Mesters, J. R.; Barinka, C.; Li, W.; Tsukamoto, T.; Majer, P.; Slusher, B. S.; Konvalinka, J.; Hilgenfeld, R. Structure of Glutamate Carboxypeptidase II, a Drug Target in Neuronal Damage and Prostate Cancer. *EMBO J.* **2006**, *25*, 1375−1384.

https://doi.org/10.1021/acsomega.1c03554
ACS Omega 2021, 6, 33354−33369

(25) Pavlicek, J.; Ptacek, J.; Barinka, C. Glutamate Carboxypeptidase II: An Overview of Structural Studies and Their Importance for Structure-Based Drug Design and Deciphering the Reaction Mechanism of the Enzyme. *Curr. Med. Chem.* **2012**, *19*, 1300−1309.
(26) O'Keefe, D. S.; Su, S. L.; Bacich, D. J.; Horiguchi, Y.; Luo, Y.; Powell, C. T.; Zandvliet, D.; Russell, P. J.; Molloy, P. L.; Nowak, N. J.; Shows, T. B.; Mullins, C.; Vonder Haar, R. A.; Fair, W. R.; Heston, W. D. W. Mapping, Genomic Organization and Promoter Analysis of the Human Prostate-specific Membrane Antigen Gene. *Biochim. Biophys. Acta, Gene Struct. Expression* **1998**, *1443*, 113−127.
(27) Kinoshita, Y.; Kuratsukuri, K.; Landas, S.; Imaida, K.; Rovito, P. M., Jr.; Wang, C. Y.; Haas, G. P. Expression of Prostate-specific Membrane Antigen in Normal and Malignant Human Tissues. *World J. Surg.* **2006**, *30*, 628−636.
(28) Silver, D. A.; Pellicer, I.; Fair, W. R.; Heston, W. D.; Cordon-Cardo, C. Prostate-specific Membrane Antigen Expression in Normal and Malignant Human Tissues. *Clin. Cancer Res.* **1997**, *3*, 81−85.
(29) Halsted, C. H.; Wong, D. H.; Peerson, J. M.; Warden, C. H.; Refsum, H.; Smith, A. D.; Nygård, O. K.; Ueland, P. M.; Vollset, S. E.; Tell, G. S. Relations of Glutamate Carboxypeptidase II (GCPII) Polymorphisms to Folate and Homocysteine Concentrations and to Scores of Cognition, Anxiety, and Depression in a Homogeneous Norwegian Population: the Hordaland Homocysteine Study. *Am. J. Clin. Nutr.* **2007**, *86*, 514−521.
(30) Devlin, A. M.; Ling, E. H.; Peerson, J. M.; Fernando, S.; Clarke, R.; Smith, A. D.; Halsted, C. H. Glutamate Carboxypeptidase II: a Polymorphism Associated with Lower Levels of Serum Folate and Hyperhomocysteinemia. *Hum. Mol. Genet.* **2000**, *9*, 2837−2844.
(31) Slusher, B. S.; Vornov, J. J.; Thomas, A. G.; Hurn, P. D.; Harukuni, I.; Bhardwaj, A.; Traystman, R. J.; Robinson, M. B.; Britton, P.; Lu, X.-C. M.; Tortella, F. C.; Wozniak, K. M.; Yudkoff, M.; Potter, B. M.; Jackson, P. F. Selective Inhibition of NAALADase, Which Converts NAAG to Glutamate, Reduces Ischemic Brain Injury. *Nat. Med.* **1999**, *5*, 1396−1402.
(32) Bacich, D. J.; Wozniak, K. M.; Lu, X.-C. M.; O'Keefe, D. S.; Callizot, N.; Heston, W. D. W.; Slusher, B. S. Mice Lacking Glutamate Carboxypeptidase II Are Protected from Peripheral Neuropathy and Ischemic Brain Injury. *J. Neurochem.* **2005**, *95*, 314−323.
(33) Neale, J. H.; Yamamoto, T. N-acetylaspartylglutamate (NAAG) and Glutamate Carboxypeptidase II: An Abundant Peptide Neurotransmitter-enzyme System with Multiple Clinical Applications. *Prog. Neurobiol.* **2020**, *184*, 101722.
(34) Tricoli, J. V.; Schoenfeldt, M.; Conley, B. A. Detection of Prostate Cancer and Predicting Progression: Current and Future Diagnostic Markers. *Clin. Cancer Res.* **2004**, *10*, 3943−3953.
(35) Hupe, M. C.; Philippi, C.; Roth, D.; Kümpers, C.; Ribbat-Idel, J.; Becker, F.; Joerg, V.; Duensing, S.; Lubczyk, V. H.; Kirfel, J.; Sailer, V.; Kuefer, R.; Merseburger, A. S.; Perner, S.; Offermann, A. Expression of Prostate-Specific Membrane Antigen (PSMA) on Biopsies Is an Independent Risk Stratifier of Prostate Cancer Patients at Time of Initial Diagnosis. *Front. Oncol.* **2018**, *8*, 623.
(36) Evans, M. J.; Smith-Jones, P. M.; Wongvipat, J.; Navarro, V.; Kim, S.; Bander, N. H.; Larson, S. M.; Sawyers, C. L. Noninvasive Measurement of Androgen Receptor Signaling with a Positron-emitting Radiopharmaceutical that Targets Prostate-specific Membrane Antigen. *Proc. Natl. Acad. Sci. U.S.A.* **2011**, *108*, 9578−9582.
(37) Bakht, M. K.; Oh, S. W.; Youn, H.; Cheon, G. J.; Kwak, C.; Kang, K. W. Influence of Androgen Deprivation Therapy on the Uptake of PSMA-Targeted Agents: Emerging Opportunities and Challenges. *Nucl. Med. Mol. Imaging* **2017**, *51*, 202−211.
(38) Kesch, C.; Kratochwil, C.; Mier, W.; Kopka, K.; Giesel, F. L. (68)Ga or (18)F for Prostate Cancer Imaging? *J. Nucl. Med.* **2017**, *58*, 687−688.
(39) Barbosa, F. G.; Queiroz, M. A.; Nunes, R. F.; Marin, J. F. G.; Buchpiguel, C. A.; Cerri, G. G. Clinical Perspectives of PSMA PET/MRI for Prostate Cancer. *Clinics* **2018**, *73*, No. e586s.
(40) Giovacchini, G.; Giovannini, E.; Riondato, M.; Ciarmiello, A. PET/CT With (68)Ga-PSMA in Prostate Cancer: Radiopharmaceutical Background and Clinical Implications. *Curr. Radiopharm.* **2018**, *11*, 4−13.
(41) Bräuer, A.; Grubert, L. S.; Roll, W.; Schrader, A. J.; Schäfers, M.; Bögemann, M.; Rahbar, K. 177Lu-PSMA-617 radioligand therapy and outcome in patients with metastasized castration-resistant prostate cancer. *Eur. J. Nucl. Med. Mol. Imaging* **2017**, *44*, 1663−1670.
(42) Fendler, W. P.; Rahbar, K.; Herrmann, K.; Kratochwil, C.; Eiber, M. 177Lu-PSMA Radioligand Therapy for Prostate Cancer. *J. Nucl. Med.* **2017**, *58*, 1196−1200.
(43) Hillier, S. M.; Maresca, K. P.; Femia, F. J.; Marquis, J. C.; Foss, C. A.; Nguyen, N.; Zimmerman, C. N.; Barrett, J. A.; Eckelman, W. C.; Pomper, M. G.; Joyal, J. L.; Babich, J. W. Preclinical Evaluation of Novel Glutamate-urea-lysine Analogues that Target Prostate-specific Membrane Antigen as Molecular Imaging Pharmaceuticals for Prostate Cancer. *Cancer Res.* **2009**, *69*, 6932−6940.
(44) Mier, W.; Gabel, D.; Haberkorn, U.; Eisenhut, M. Conjugation of the Closo-borane Mercaptoundecahydrododecaborate (BSH) to a Tumour Selective Peptide. *Anorg. Allg. Chem.* **2004**, *630*, 1258−1262.
(45) Wei, X.; Shao, B.; He, Z.; Ye, T.; Luo, M.; Sang, Y.; Liang, X.; Wang, W.; Luo, S.; Yang, S.; Zhang, S.; Gong, C.; Gou, M.; Deng, H.; Zhao, Y.; Yang, H.; Deng, S.; Zhao, C.; Yang, L.; Qian, Z.; Li, J.; Sun, X.; Han, J.; Jiang, C.; Wu, M.; Zhang, Z. Cationic Nanocarriers Induce Cell Necrosis Through Impairment of Na+/K+-ATPase and Cause Subsequent Inflammatory Response. *Cell Res.* **2015**, *25*, 237−253.
(46) Mi, P.; Yanagie, H.; Dewi, N.; Yen, H.-C.; Liu, X.; Suzuki, M.; Sakurai, Y.; Ono, K.; Takahashi, H.; Cabral, H.; Kataoka, K.; Nishiyama, N. Block Copolymer-boron Cluster Conjugate for Effective Boron Neutron Capture Therapy of Solid Tumors. *J. Controlled Release* **2017**, *254*, 1−9.
(47) Ito, Y.; Kimura, Y.; Shimahara, T.; Ariyoshi, Y.; Shimahara, M.; Miyatake, S.; Kawabata, S.; Kasaoka, S.; Ono, K. Disposition of TF-PEG-Liposome-BSH in Tumor-bearing Mice. *Appl. Radiat. Isot.* **2009**, *67*, S109−S110.
(48) Zhu, Y.; Koh Cheng, Y.; John, A. M.; Narayan, S. H. Recent Developments in Boron Neutron Capture Therapy (BNCT) Driven by Nanotechnology. *Curr. Chem. Biol.* **2007**, *1*, 141−149.
(49) Demirkol, M. O.; Acar, Ö.; Uçar, B.; Ramazanoğlu, S. R.; Sağlıcan, Y.; Esen, T. Prostate-specific Membrane Antigen-based Imaging in Prostate Cancer: Impact on Clinical Decision Making Process. *Prostate* **2015**, *75*, 748−757.
(50) Osborne, J. R.; Akhtar, N. H.; Vallabhajosula, S.; Anand, A.; Deh, K.; Tagawa, S. T. Prostate-specific Membrane Antigen-based Imaging. *Urol. Oncol.* **2013**, *31*, 144−154.
(51) Rahbar, K.; Afshar-Oromieh, A.; Jadvar, H.; Ahmadzadehfar, H. PSMA Theranostics: Current Status and Future Directions. *Mol. Imaging* **2018**, *17*, 1536012118776068.
(52) Mukherjee, A.; Kumar, B.; Hatano, K.; Russell, L. M.; Trock, B. J.; Searson, P. C.; Meeker, A. K.; Pomper, M. G.; Lupold, S. E. Development and Application of a Novel Model System to Study "Active" and "Passive" Tumor Targeting. *Mol. Cancer Ther.* **2016**, *15*, 2541−2550.
(53) Davis, M. I.; Bennett, M. J.; Thomas, L. M.; Bjorkman, P. J. Crystal Structure of Prostate-specific Membrane Antigen, a Tumor Marker and Peptidase. *Proc. Natl. Acad. Sci. U.S.A.* **2005**, *102*, 5981−5986.
(54) Barinka, C.; Hlouchova, K.; Rovenska, M.; Majer, P.; Dauter, M.; Hin, N.; Ko, Y.-S.; Tsukamoto, T.; Slusher, B. S.; Konvalinka, J.; Lubkowski, J. Structural Basis of Interactions between Human Glutamate Carboxypeptidase II and Its Substrate Analogs. *J. Mol. Biol.* **2008**, *376*, 1438−1450.
(55) Tykvart, J.; Schimer, J.; Bařinková, J.; Pachl, P.; Poštová-Slavětínská, L.; Majer, P.; Konvalinka, J.; Šácha, P. Rational Design of Urea-based Glutamate Carboxypeptidase II (GCPII) Inhibitors as Versatile Tools for Specific Drug Targeting and Delivery. *Bioorg. Med. Chem.* **2014**, *22*, 4099−4108.
(56) Pandit, A.; Sengupta, S.; Krishnan, M. A.; Reddy, R. B.; Sharma, R.; Venkatesh, C. First Report on 3D-QSAR and Molecular Dynamics

https://doi.org/10.1021/acsomega.1c03554
ACS Omega 2021, 6, 33354−33369

Based Docking Studies of GCPII Inhibitors for Targeted Drug Delivery Applications. *J. Mol. Struct.* **2018**, *1159*, 179−192.
(57) Barinka, C.; Novakova, Z.; Hin, N.; Bím, D.; Ferraris, D. V.; Duvall, B.; Kabarriti, G.; Tsukamoto, R.; Budesinsky, M.; Motlova, L.; Rojas, C.; Slusher, B. S.; Rokob, T. A.; Rulíšek, L.; Tsukamoto, T. Structural and Computational Basis for Potent Inhibition of Glutamate Carboxypeptidase II by Carbamate-based Inhibitors. *Bioorg. Med. Chem.* **2019**, *27*, 255−264.
(58) Wüstemann, T.; Haberkorn, U.; Babich, J.; Mier, W. Targeting Prostate Cancer: Prostate-specific Membrane Antigen Based Diagnosis and Therapy. *Med. Res. Rev.* **2019**, *39*, 40−69.
(59) Pavlicek, J.; Ptacek, J.; Cerny, J.; Byun, Y.; Skultetyova, L.; Pomper, M. G.; Lubkowski, J.; Barinka, C. Structural Characterization of P1'-diversified Urea-based Inhibitors of Glutamate Carboxypeptidase II. *Bioorg. Med. Chem. Lett.* **2014**, *24*, 2340−2345.
(60) Youn, S.; Kim, K. I.; Ptacek, J.; Ok, K.; Novakova, Z.; Kim, Y.; Koo, J.; Barinka, C.; Byun, Y. Carborane-containing Urea-based Inhibitors of Glutamate Carboxypeptidase II: Synthesis and Structural Characterization. *Bioorg. Med. Chem. Lett.* **2015**, *25*, 5232−5236.
(61) Barinka, C.; Byun, Y.; Dusich, C. L.; Banerjee, S. R.; Chen, Y.; Castanares, M.; Kozikowski, A. P.; Mease, R. C.; Pomper, M. G.; Lubkowski, J. Interactions Between Human Glutamate Carboxypeptidase II and Urea-based Inhibitors: Structural Characterization. *J. Med. Chem.* **2008**, *51*, 7737−7743.
(62) Kozikowski, A. P.; Nan, F.; Conti, P.; Zhang, J.; Ramadan, E.; Bzdega, T.; Wroblewska, B.; Neale, J. H.; Pshenichkin, S.; Wroblewski, J. T. Design of Remarkably Simple, Yet Potent Urea-Based Inhibitors of Glutamate Carboxypeptidase II (NAALADase). *J. Med. Chem.* **2001**, *44*, 298−301.
(63) Ferraris, D. V.; Shukla, K.; Tsukamoto, T. Structure-Activity Relationships of Glutamate Carboxypeptidase II (GCPII) Inhibitors. *Curr. Med. Chem.* **2012**, *19*, 1282−1294.
(64) Wirtz, M.; Schmidt, A.; Schottelius, M.; Robu, S.; Günther, T.; Schwaiger, M.; Wester, H.-J. Synthesis and in Vitro and in Vivo Evaluation of Urea-based PSMA Inhibitors with Increased Lipophilicity. *EJNMMI Res.* **2018**, *8*, 84.
(65) Koerber, S. A.; Will, L.; Kratochwil, C.; Haefner, M. F.; Rathke, H.; Kremer, C.; Merkle, J.; Herfarth, K.; Kopka, K.; Choyke, P. L.; Holland-Letz, T.; Haberkorn, U.; Debus, J.; Giesel, F. L. (68)Ga-PSMA-11 PET/CT in Primary and Recurrent Prostate Carcinoma: Implications for Radiotherapeutic Management in 121 Patients. *J. Nucl. Med.* **2018**, *60*, 234.
(66) El-Zaria, M. E.; Genady, A. R.; Janzen, N.; Petlura, C. I.; Beckford Vera, D. R.; Valliant, J. F. Preparation and Evaluation of Carborane-derived Inhibitors of Prostate Specific Membrane Antigen (PSMA). *Dalton Trans.* **2014**, *43*, 4950−4961.
(67) Wang, S.; Blaha, C.; Santos, R.; Huynh, T.; Hayes, T. R.; Beckford-Vera, D. R.; Blecha, J. E.; Hong, A. S.; Fogarty, M.; Hope, T. A.; Raleigh, D. R.; Wilson, D. M.; Evans, M. J.; VanBrocklin, H. F.; Ozawa, T.; Flavell, R. R. Synthesis and Initial Biological Evaluation of Boron-Containing Prostate-Specific Membrane Antigen Ligands for Treatment of Prostate Cancer Using Boron Neutron Capture Therapy. *Mol. Pharm.* **2019**, *16*, 3831−3841.
(68) Mesters, J. R.; Henning, K.; Hilgenfeld, R. Human Glutamate Carboxypeptidase II Inhibition: Structures of GCPII in Complex with Two Potent Inhibitors, Quisqualate and 2-PMPA. *Acta Crystallogr., Sect. D: Biol. Crystallogr.* **2007**, *63*, 508−513.
(69) Sharma, G.; Hu, Q.; Jayasinghe-Arachchige, V. M.; Paul, T. J.; Schenk, G.; Prabhakar, R. Investigating Coordination Flexibility of Glycerophosphodiesterase (GpdQ) Through Interactions with Mono-, Di-, and Triphosphoester (NPP, BNPP, GPE, and paraoxon) Substrates. *Phys. Chem. Chem. Phys.* **2019**, *21*, 5499−5509.
(70) Hu, Q.; Jayasinghe-Arachchige, V. M.; Sharma, G.; Serafim, L. F.; Paul, T. J.; Prabhakar, R. Mechanisms of Peptide and Phosphoester Hydrolysis Catalyzed by Two Promiscuous Metalloenzymes (Insulin Degrading Enzyme and Glycerophosphodiesterase) and Their Synthetic Analogues. *Wires Comput. Mol. Sci.* **2020**, *10*, No. e1466.
(71) Paul, F. J.; Barbara, S. S. Design of NAALADase Inhibitors: A Novel Neuroprotective Strategy. *Curr. Med. Chem.* **2001**, *8*, 949−957.
(72) Robinson, M. B.; Blakely, R. D.; Couto, R.; Coyle, J. T. Hydrolysis of the Brain Dipeptide N-acetyl-L-aspartyl-L-glutamate. Identification and Characterization of a Novel N-acetylated Alpha-linked Acidic Dipeptidase Activity from Rat Brain. *J. Biol. Chem.* **1987**, *262*, 14498−14506.
(73) Yung-Chi, C.; Prusoff, W. H. Relationship Between the Inhibition Constant (KI) and the Concentration of Inhibitor Which Causes 50 Per Cent Inhibition (I50) of an Enzymatic Reaction. *Biochem. Pharmacol.* **1973**, *22*, 3099−3108.
(74) Shen, W.; Li, M.; Li, Y.; Wang, S. Theoretical Study of Borazine and Its Derivatives. *Inorg. Chim. Acta* **2007**, *360*, 619−624.
(75) Islas, R.; Chamorro, E.; Robles, J.; Heine, T.; Santos, J. C.; Merino, G. Borazine: to Be or not to Be Aromatic. *Struct. Chem.* **2007**, *18*, 833−839.
(76) Haberecht, M. C.; Bolte, M.; Wagner, M.; Lerner, H.-W. A New Polymorph of Tri(p-tolyl)boroxine. *J. Chem. Crystallogr.* **2005**, *35*, 657−665.
(77) Grimes, R. N. Structure and Bonding. In *Carboranes*, 3rd ed.; Grimes, R. N., Ed.; Academic Press: Boston, 2016; Chapter 2, pp 7−18.
(78) Wade, K. The Structural Significance of the Number of Skeletal Bonding Electron-pairs in Carboranes, the Higher Boranes and Borane Anions, and Various Transition-metal Carbonyl Cluster Compounds. *J. Chem. Soc. D* **1971**, *15*, 792−793.
(79) Mingos, D. M. P. A General Theory for Cluster and Ring Compounds of the Main Group and Transition Elements. *Nat. Phys. Sci.* **1972**, *236*, 99−102.
(80) Bendová, L.; Jurečka, P.; Hobza, P.; Vondrášek, J. Model of Peptide Bond-Aromatic Ring Interaction:Correlated Ab Initio Quantum Chemical Study. *J. Phys .Chem .B* **2007**, *111*, 9975−9979.
(81) Nishio, M.; Hirota, M.; Umezawa, Y. *The CH/pi Interaction*; Wiley-VCH: New York, 1998.
(82) Becke, A. D. Density-functional Thermochemistry. III. The Role of Exact Exchange. *J. Chem. Phys.* **1993**, *98*, 5648−5652.
(83) Francl, M. M.; Pietro, W. J.; Hehre, W. J.; Binkley, J. S.; Gordon, M. S.; DeFrees, D. J.; Pople, J. A. Self-consistent Molecular Orbital Methods. XXIII. A Polarization-type Basis Set for Second-row Elements. *J. Chem. Phys.* **1982**, *77*, 3654−3665.
(84) Frisch, M. J.; Trucks, G. W.; Schlegel, H. B.; Scuseria, G. E.; Robb, M. A.; Cheeseman, J. R.; Scalmani, G.; Barone, V.; Mennucci, B.; Petersson, G. A.; Nakatsuji, H.; Caricato, M.; Li, X.; Hratchian, H. P.; Izmaylov, A. F.; Bloino, J.; Zheng, G.; Sonnenberg, J. L.; Hada, M.; Ehara, M.; Toyota, K.; Fukuda, R.; Hasegawa, J.; Ishida, M.; Nakajima, T.; Honda, Y.; Kitao, O.; Nakai, H.; Vreven, T.; Montgomery, J. A.; Peralta, J. E.; Ogliaro, F.; Bearpark, M.; Heyd, J. J.; Brothers, E.; Kudin, K. N.; Staroverov, V. N.; Kobayashi, R.; Normand, J.; Raghavachari, K.; Rendell, A.; Burant, J. C.; Iyengar, S. S.; Tomasi, J.; Cossi, M.; Rega, N.; Millam, J. M.; Klene, M.; Knox, J. E.; Cross, J. B.; Bakken, V.; Adamo, C.; Jaramillo, J.; Gomperts, R.; Stratmann, R. E.; Yazyev, O.; Austin, A. J.; Cammi, R.; Pomelli, C.; Ochterski, J. W.; Martin, R. L.; Morokuma, K.; Zakrzewski, V. G.; Voth, G. A.; Salvador, P.; Dannenberg, J. J.; Dapprich, S.; Daniels, A. D.; Farkas; Foresman, J. B.; Ortiz, J. V.; Cioslowski, J.; Fox, D. J., *Gaussian 09*, Revision D.01; Gaussian, Inc.: Wallingford CT, 2009.
(85) Malde, A. K.; Zuo, L.; Breeze, M.; Stroet, M.; Poger, D.; Nair, P. C.; Oostenbrink, C.; Mark, A. E. An Automated Force Field Topology Builder (ATB) and Repository: Version 1.0. *J. Chem. Theory Comput.* **2011**, *7*, 4026−4037.
(86) Trott, O.; Olson, A. J. AutoDock Vina: Improving the Speed and Accuracy of Docking with a New Scoring Function, Efficient Optimization, and Multithreading. *J. Comput. Chem.* **2010**, *31*, 455−61.
(87) Hess, B.; Kutzner, C.; van der Spoel, D.; Lindahl, E. GROMACS 4:Algorithms for Highly Efficient ,Load -Balanced,and Scalable Molecular Simulation. *J .Chem .Theory Comput .* **2008**, *4*, 435−447.

https://doi.org/10.1021/acsomega.1c03554
ACS Omega 2021, 6, 33354−33369

(88) Schmid, N.; Eichenberger, A. P.; Choutko, A.; Riniker, S.; Winger, M.; Mark, A. E.; van Gunsteren, W. F. Definition and Testing of the GROMOS Force-field Versions 54A7 and 54B7. *Eur. Biophys. J.* **2011**, *40*, 843−856.
(89) de Souza, O. N.; Ornstein, R. L. Effect of Periodic Box Size on Aqueous Molecular Dynamics Simulation of a DNA Dodecamer with Particle-mesh Ewald Method. *Biophys. J.* **1997**, *72*, 2395−2397.
(90) Toukan, K.; Rahman, A. Molecular-dynamics Study of Atomic Motions in Water. *Phys. Rev. B: Condens. Matter Mater.* **1985**, *31*, 2643−2648.
(91) Hess, B.; Bekker, H.; Berendsen, H. J. C.; Fraaije, J. G. E. M. LINCS: A Linear Constraint Solver for Molecular Simulations. *J. Comput. Chem.* **1997**, *18*, 1463−1472.
(92) Miyamoto, S.; Kollman, P. A. Settle: An Analytical Version of the SHAKE and RATTLE Algorithm for Rigid Water Models. *J. Comput. Chem.* **1992**, *13*, 952−962.
(93) Darden, T.; York, D.; Pedersen, L. Particle Mesh Ewald: An N·log(N) Method for Ewald Sums in Large Systems. *J. Chem. Phys.* **1993**, *98*, 10089−10092.
(94) Michaud-Agrawal, N.; Denning, E. J.; Woolf, T. B.; Beckstein, O. MDAnalysis: A Toolkit for the Analysis of Molecular Dynamics Simulations. *J. Comput. Chem.* **2011**, *32*, 2319−2327.
(95) Knight, J. L.; Brooks, C. L. λ-Dynamics free energy simulation methods. *J. Comput. Chem.* **2009**, *30*, 1692−1700.
(96) Kong, X.; Brooks, C. L. λ-dynamics: A new approach to free energy calculations. *J. Chem. Phys.* **1996**, *105*, 2414−2423.
(97) Guo, Z.; Brooks, C. L.; Kong, X. Efficient and Flexible Algorithm for Free Energy Calculations Using the λ-Dynamics Approach. *J. Phys. Chem. B* **1998**, *102*, 2032−2036.
(98) Steinbrecher, T.; Joung, I.; Case, D. A. Soft-core Potentials in Thermodynamic Integration: Comparing One- and Two-step Transformations. *J. Comput. Chem.* **2011**, *32*, 3253−3263.
(99) Contreras-García, J.; Johnson, E. R.; Keinan, S.; Chaudret, R.; Piquemal, J.-P.; Beratan, D. N.; Yang, W. NCIPLOT: A Program for Plotting Noncovalent Interaction Regions. *J. Chem. Theory Comput.* **2011**, *7*, 625−632.
(100) Kabsch, W.; Sander, C. Dictionary of Protein Secondary Structure: Pattern Recognition of Hydrogen-bonded and Geometrical Features. *Biopolymers* **1983**, *22*, 2577−2637.
(101) Baker, N. A.; Sept, D.; Joseph, S.; Holst, M. J.; McCammon, J. A. Electrostatics of Nanosystems: Application to Microtubules and the Ribosome. *Proc. Natl. Acad. Sci. U.S.A.* **2001**, *98*, 10037−10041.
(102) Schrödinger, L. L. C. *PyMOL Molecular Graphics System*, version 1.8; Schrodinger LLC: New York, 2015.
(103) Humphrey, W.; Dalke, A.; Schulten, K. VMD: Visual Molecular Dynamics. *J. Mol. Graphics* **1996**, *14*, 33−38.
(104) Cousins, K. R. ChemDraw Ultra 9.0. CambridgeSoft, 100 CambridgePark Drive, Cambridge, MA 02140. www.cambridgesoft.-com. See Web Site for Pricing Options. *J. Am. Chem. Soc.* **2005**, *127*, 4115−4116.
(105) Krieger, E.; Vriend, G. YASARA View—Molecular Graphics for All Devices - from Smartphones to Workstations. *Bioinformatics* **2014**, *30*, 2981−2982.
(106) Pettersen, E. F.; Goddard, T. D.; Huang, C. C.; Couch, G. S.; Greenblatt, D. M.; Meng, E. C.; Ferrin, T. E. UCSF Chimera?A visualization system for exploratory research and analysis. *J. Comput. Chem.* **2004**, *25*, 1605−1612.
(107) Lever, J.; Krzywinski, M.; Altman, N. Principal Component Analysis. *Nat. Methods* **2017**, *14*, 641−642.
(108) Ichiye, T.; Karplus, M. Collective Motions in Proteins: A Covariance Analysis of Atomic Fluctuations in Molecular Dynamics and Normal Mode Simulations. *Proteins* **1991**, *11*, 205−217.

https://doi.org/10.1021/acsomega.1c03554
ACS Omega 2021, 6, 33354−33369